CHAPTER 7 FINITE ELEMENT ANALYSIS OF END FRICTION

Introduction

Since attempts at closed form solutions to the restrained cylinder problem have been relatively unsuccessful, and since only one attempt characterized the degree of restraint as other than complete (no lateral deformation at ends), finite element analyses of a triaxial test specimen subjected to varying degrees of friction on its ends were undertaken. These analyses were conducted to investigate the influence of various levels of friction on the interface on stress distributions in the specimen, differences in the measured and actual stress-strain response, and the shear stresses in the specimen at steady state conditions.

The friction between the end platens and the specimen results in a shear stress on the plane ends of the specimen acting in the radial direction toward the specimen axis as deformation progresses. This shear stress has several effects: it increases the confining stress of the material in the regions near the specimen ends, it induces a stress concentration at the intersection of the ends and the cylindrical surface of the specimen, and it rotates the principal stresses in the specimen near the ends. The increase in confining stress can result in an increase in shear strength in the regions of the specimen affected, and can result in an overprediction of strength. The induced shear stresses and the rotation of principal stresses result in an underprediction of the actual deviator stress in the region of the specimen affected since it is assumed that the major principal stress throughout the specimen is oriented along the axis of the specimen. Localized failure may occur in the vicinity of the end platens prior to specimen failure since the actual deviator stress is greater than the measured or average deviator stress in this region. Therefore, the error introduced into

the measured stress level whenever localized principal stress rotation occurs in the specimen can result in an underprediction of strength. The overall effect of these combined factors on measured stress-strain response and shear strength parameters is dependent on the material properties, interface characteristics, testing conditions, and degree of deformation in the specimen. The finite element analyses evaluated this effect for a variety of these conditions.

Axisymmetric analyses that employed axisymmetric interface elements to model the friction between the specimen and the end platens were conducted. Various material models were used to simulate the test specimen, including linear elastic, nonlinear elastic, and nonlinear elasto-plastic constitutive models. The finite element computer program SAGE, developed at Virginia Tech to model soil structure interaction problems (Morrison 1995), was modified to satisfy the requirements for this research effort. The necessary changes included conversion of the plane strain version to an axisymmetric formulation and the addition of the axisymmetric interface elements. SAGE was chosen primarily because of its modularity. The programming style adopted during the development of SAGE code facilitated the addition of various material models and new elements (Morrison 1995).

Finite Element Problem Formulation

The most common method of finite element formulation for structural analysis is the minimization of a potential energy functional (Cook et al. 1989, Zienkiewicz and Taylor 1989). This functional describes the potential energy of a body in terms of displacements, and can be defined as:

$$\Pi_P = U + \Omega \qquad \text{Equation 7.1}$$

where: Π_P = potential energy of the body
U = strain energy
Ω = external work (potential of loads)

The correct displacements throughout the body of interest are those that minimize the potential energy of the body. The minimum potential energy corresponds to the displacements for which the variation of the potential energy with respect to displacement is zero. This variation is defined by:

$$d\Pi_P = \frac{\partial \Pi_P}{\partial D_1} dD_1 + \frac{\partial \Pi_P}{\partial D_2} dD_2 + \ldots + \frac{\partial \Pi_P}{\partial D_n} dD_n = 0 \qquad \text{Equation 7.2}$$

Since the displacements D_i in Equation 7.2 are thus far arbitrary, the requirement is satisfied only if each of the derivatives in Equation 7.2 is equal to zero. Thus, the governing equation for the finite element solution based on the minimization of the potential energy is:

$$\frac{\partial \Pi_P}{\partial D_i} = 0 \qquad \text{Equation 7.3}$$

The strain energy of the body and the external work done can be described by:

$$U = \int_V \tfrac{1}{2} \{\boldsymbol{\varepsilon}\}^{\mathrm{T}} [\mathbf{E}] \{\boldsymbol{\varepsilon}\} dV \qquad \text{Equation 7.4}$$

$$\Omega = -\int_V \{\boldsymbol{\varepsilon}\}^{\mathrm{T}} [\mathbf{E}] \{\boldsymbol{\varepsilon}_0\} dV + \int_V \{\boldsymbol{\varepsilon}\}^{\mathrm{T}} \{\boldsymbol{\sigma}_0\} dV - \int_V \{\mathbf{u}\}^{\mathrm{T}} \{\mathbf{F}\} dV - \int_S \{\mathbf{u}\}^{\mathrm{T}} \{\boldsymbol{\Phi}\} dS \qquad \text{Equation 7.5}$$

where:
- $\{\boldsymbol{\varepsilon}\}$ = strain vector
- $[\mathbf{E}]$ = constitutive matrix relating strain vector to stress vector
- $\{\boldsymbol{\varepsilon}_0\}$ = initial strain vector
- $\{\boldsymbol{\sigma}_0\}$ = initial stress vector
- $\{\mathbf{u}\}$ = displacement vector
- $\{\mathbf{F}\}$ = body force vector
- $\{\boldsymbol{\Phi}\}$ = surface traction vector

The body or continuum is discretized into a system of nodes and elements so that expressions may be written for the strain energy and the external work in terms of nodal quantities and interpolation functions. The interpolation of

displacements and strains is accomplished using an interpolation function matrix and the nodal displacement vector:

$$\{\mathbf{u}\} = [\mathbf{N}]\{\mathbf{D}\}$$ Equation 7.6

$$\{\boldsymbol{\varepsilon}\} = [\partial]\{\mathbf{u}\} = [\partial][\mathbf{N}]\{\mathbf{D}\} = [\mathbf{B}]\{\mathbf{D}\}$$ Equation 7.7

where: $[\mathbf{N}]$ = interpolation function matrix
$\{\mathbf{D}\}$ = nodal displacement vector
$[\partial]$ = differential operator matrix
$[\mathbf{B}]$ = $[\partial][\mathbf{N}]$

The interpolation functions can be used to interpolate other quantities such as initial stresses, initial strains, and body and traction forces based on nodal values as well. Equation 7.4 and Equation 7.5 can be rewritten in terms of the nodal quantities as follows:

$$U = \tfrac{1}{2}\{\mathbf{D}\}^{\mathrm{T}}\left(\int_V [\mathbf{B}]^{\mathrm{T}}[\mathbf{E}][\mathbf{B}]dV\right)\{\mathbf{D}\}$$ Equation 7.8

$$\Omega = -\{\mathbf{D}\}^{\mathrm{T}}\left(\int_V [\mathbf{B}]^{\mathrm{T}}[\mathbf{E}]\{\boldsymbol{\varepsilon}_0\}dV - \int_V [\mathbf{B}]^{\mathrm{T}}\{\boldsymbol{\sigma}_0\}dV + \int_V [\mathbf{N}]^{\mathrm{T}}\{\mathbf{F}\}dV\right) - \{\mathbf{D}\}^{\mathrm{T}}\int_S [\mathbf{N}]^{\mathrm{T}}\{\boldsymbol{\Phi}\}dS - \{\mathbf{D}\}^{\mathrm{T}}\{\mathbf{P}\}$$
Equation 7.9

Introducing the stiffness matrix and the nodal load vector, the expressions can be simplified as follows:

$$U = \tfrac{1}{2}\{\mathbf{D}\}^{\mathrm{T}}[\mathbf{K}]\{\mathbf{D}\}$$ Equation 7.10

$$\Omega = -\{\mathbf{D}\}^{\mathrm{T}}\{\mathbf{R}\}$$ Equation 7.11

where: $[\mathbf{K}]$ = stiffness matrix
$\{\mathbf{R}\}$ = vector of nodal lodes

The potential energy of the body can now be written as:

$$\Pi_P = \tfrac{1}{2}\{\mathbf{D}\}^{\mathrm{T}}[\mathbf{K}]\{\mathbf{D}\} - \{\mathbf{D}\}^{\mathrm{T}}\{\mathbf{R}\}$$

and the governing equation is:

$$\frac{\partial \Pi_P}{\partial D_i} = [\mathbf{K}]\{\mathbf{D}\} - \{\mathbf{R}\} = 0$$

$$[\mathbf{K}]\{\mathbf{D}\} = \{\mathbf{R}\}$$

where the stiffness matrix is defined by:

$$[\mathbf{K}] = \iiint_V [\mathbf{B}]^{\mathrm{T}}[\mathbf{E}][\mathbf{B}]dV \qquad \text{Equation 7.12}$$

and the equivalent nodal load vector is defined by:

$$\{\mathbf{R}\} = \int_V [\mathbf{B}]^{\mathrm{T}}[\mathbf{E}]\{\boldsymbol{\varepsilon}_0\}dV - \int_V [\mathbf{B}]^{\mathrm{T}}\{\boldsymbol{\sigma}_0\}dV + \int_V [\mathbf{N}]^{\mathrm{T}}\{\mathbf{F}\}dV + \int_S [\mathbf{N}]^{\mathrm{T}}\{\boldsymbol{\Phi}\}dS + \{\mathbf{P}\}$$

Equation 7.13

where the terms account for, respectively, initial strains, initial stresses, body forces, surface tractions, and point loads on the body. The transformations and mapping functions required in order to integrate the required expressions based on nodal quantities and interpolation functions for both plane strain and axisymmetric formulations are discussed in more detail in Appendix D. The major difference in integration for the axisymmetric formulation is that the thickness of the body, which is constant for plane strain, varies with the radial coordinate for axisymmetric problems. As a result, the volume integrals must be evaluated using a *thickness* of $2\pi r$ rather than a unit thickness. Since the radial coordinate will in general vary across the mesh, the integrals are more complex due to the additional interpolation required to evaluate each integrand.

In addition to the differences in integration for plane strain and axisymmetric formulations, the stress and strain vectors, the constitutive matrix, and the $\mathbf{B}$ matrix differ as well. The constitutive relationship for a linearly elastic material is described by:

$$\{\sigma\} = [\mathbf{E}]\{\varepsilon\}$$

For plane strain conditions, the stress, strain, and constitutive matrices for a linear elastic material can be described as follows (after Zienkiewicz and Taylor 1989):

$$\{\boldsymbol{\sigma}\} = \begin{Bmatrix} \sigma_x \\ \sigma_y \\ \sigma_z \\ \tau_{xy} \end{Bmatrix} \qquad \{\boldsymbol{\varepsilon}\} = \begin{Bmatrix} \varepsilon_x \\ \varepsilon_y \\ \gamma_{xy} \end{Bmatrix}$$

$$[\mathbf{E}] = \frac{E}{(1+\nu)(1-2\nu)} \begin{bmatrix} 1-\nu & \nu & 0 \\ \nu & 1-\nu & 0 \\ \nu & \nu & 0 \\ 0 & 0 & \frac{1-2\nu}{2} \end{bmatrix}$$

The $\mathbf{B}$ matrix, which is used to interpolate strains based on nodal displacements is:

$$[\mathbf{B}] = \begin{bmatrix} \frac{\partial}{\partial x} & 0 \\ 0 & \frac{\partial}{\partial y} \\ \frac{\partial}{\partial y} & \frac{\partial}{\partial x} \end{bmatrix} [\mathbf{N}]$$

For axisymmetric conditions, the stress, strain, and constitutive matrices for a linear elastic material can be described as follows (after Zienkiewicz and Taylor 1989):

$$\{\boldsymbol{\sigma}\} = \begin{Bmatrix} \sigma_r \\ \sigma_z \\ \sigma_\theta \\ \tau_{rz} \end{Bmatrix} \qquad \{\boldsymbol{\varepsilon}\} = \begin{Bmatrix} \varepsilon_r \\ \varepsilon_z \\ \varepsilon_\theta \\ \gamma_{rz} \end{Bmatrix}$$

$$[\mathbf{E}] = \frac{E}{(1+\nu)(1-2\nu)} \begin{bmatrix} 1-\nu & \nu & \nu & 0 \\ \nu & 1-\nu & \nu & 0 \\ \nu & \nu & 1-\nu & 0 \\ 0 & 0 & 0 & \frac{1-2\nu}{2} \end{bmatrix}$$

The $\mathbf{B}$ matrix for axisymmetric conditions is:

$$[\mathbf{B}] = \begin{bmatrix} \frac{\partial}{\partial r} & 0 \\ 0 & \frac{\partial}{\partial z} \\ \frac{1}{r} & 0 \\ \frac{\partial}{\partial z} & \frac{\partial}{\partial r} \end{bmatrix} [\mathbf{N}]$$

Based on the differences in constituent matrices and vectors noted above and the differences in integration described in Appendix D, the axisymmetric formulation of SAGE was developed based on the plane strain version.

Interface Elements

When modeling surfaces across which the displacements are discontinuous, special finite elements, usually called *interface elements*, can be used. Goodman et al. (1968) developed the first of this type of element in order to

model discontinuous joints in rock masses. This element is based on a typical four-noded two-dimensional element, but having zero thickness. In other words, only two sets of nodal coordinates are used to define four nodes. The element was formulated based on the relative displacements occurring between the nodes with identical coordinates. While Goodman et al. (1968) developed the interface element specifically for conditions of plane strain, in the discussion that follows, a more general approach is taken so as to demonstrate the use of this type of element for axisymmetric analysis. The development of the element is based on the concepts of Goodman et al. (1968), but also follows the formulation of a mapped isoparametric interface element developed by Beer (1985).

Axisymmetric, Mapped, Isoparametric Interface Element

The relative displacements are related to stresses in the element based on a simple material property matrix as follows:

$$\begin{Bmatrix} \tau_s \\ \sigma_n \end{Bmatrix} = \begin{bmatrix} k_s & 0 \\ 0 & k_n \end{bmatrix} \begin{Bmatrix} w_s \\ w_n \end{Bmatrix} \qquad \text{Equation 7.14}$$

where:
- τ_s = shear stress tangent to the element orientation
- σ_n = normal stress perpendicular to the element orientation
- k_s = shear stiffness of the interface
- k_n = normal stiffness of the interface
- w_s = relative displacement in the shear (tangent) direction
- w_n = relative displacement in the normal (perpendicular) direction

Goodman et al. (1968) assumed that the stiffness in both directions was constant, except that if the relative normal displacement is such that the normal stress would be tensile, both stiffnesses are set equal to zero. It should be noted that the development of the element is equally valid if all terms in the material property matrix are nonzero. The effect of having the zero terms in the material property matrix used by Goodman et al. (1968) is that the shear

and normal stress displacement behaviors are uncoupled. No shear stresses develop as a result of normal displacements and no normal stresses develop as a result of shear displacements. This also implies that dilation of the interface does not occur as a result of shear displacement along the interface.

Based on Equation 7.14, which defines the stress-relative displacement relationship at a point, the potential energy of the interface can be written at a point, then integrated over the area of the contact surface to obtain the total potential energy.

$$\Pi_p = \tfrac{1}{2}\int_A \{\mathbf{w}\}^{\mathrm{T}}[\mathbf{k}]\{\mathbf{w}\}dA \qquad \text{Equation 7.15}$$

where: $[\mathbf{k}] = \begin{bmatrix} k_s & 0 \\ 0 & k_n \end{bmatrix}$

$\{\mathbf{w}\} = \begin{Bmatrix} w_s \\ w_n \end{Bmatrix}$

The relative displacements in the shear and normal directions are determined from the relative displacements in the x and y direction by means of a transformation, or rotation matrix, as follows:

$$\{\mathbf{w}\} = \begin{bmatrix} \dfrac{\partial x}{\partial s} & \dfrac{\partial x}{\partial n} \\ \dfrac{\partial y}{\partial s} & \dfrac{\partial y}{\partial n} \end{bmatrix}^{-1} \begin{Bmatrix} \Delta x \\ \Delta y \end{Bmatrix} = [\mathbf{T}]\begin{Bmatrix} \Delta x \\ \Delta y \end{Bmatrix} \qquad \text{Equation 7.16}$$

where: Δx = relative displacement in the x direction at any point
Δy = relative displacement in the y direction at any point
$[\mathbf{T}]$ = transformation matrix

The transformation matrix is sometimes referred to as the direction cosine matrix, since it relates the direction cosines between the x, y coordinate system

and the s, n coordinate system. For zero-thickness interface elements that are not curved, the transformation matrix is constant along the interface. For an element oriented in the direction of the x-axis (horizontally), the transformation matrix is simply an identity matrix. If the element is oriented along, the y axis (vertically), the diagonal terms are zero and one of the off-diagonal terms is 1 and one is -1, depending on the assumed rotation from horizontal (clockwise or counterclockwise).

The relative displacements in the x and y directions (Δx and Δy, respectively) at any point are interpolated from the nodal values of displacements using standard linear Lagrangian interpolation for one dimension. Since the two pairs of nodes share coordinates, all of the quantities to be determined only vary in one direction, along the interface element, so one-dimensional interpolation is used. If the nodes are numbered in a conventional manner (counterclockwise), and nodes 1 and 4 have identical coordinates and nodes 2 and 3 have identical coordinates, the interpolation of the relative displacements is defined by:

$$\begin{Bmatrix} \Delta x \\ \Delta y \end{Bmatrix} = \left[\mathbf{N}^{\mathbf{RD}}\right]\{\mathbf{d}\} \qquad \text{Equation 7.17}$$

where: $$\left[\mathbf{N}^{\mathbf{RD}}\right] = \begin{bmatrix} -N_1 & 0 & -N_2 & 0 & N_2 & 0 & N_1 & 0 \\ 0 & -N_1 & 0 & -N_2 & 0 & N_2 & 0 & N_1 \end{bmatrix}$$

$$\{\mathbf{d}\} = \begin{Bmatrix} u_1 \\ v_1 \\ u_2 \\ v_2 \\ u_3 \\ v_3 \\ u_4 \\ v_4 \end{Bmatrix}$$

The matrix $\left[\mathbf{N}^{\mathbf{RD}}\right]$ contains the standard linear Lagrangian interpolation functions in one dimension. The vector $\{\mathbf{d}\}$ is the vector of nodal displacements in the x and y directions. Combining Equation 7.15, Equation 7.16, and Equation 7.17, and remembering that the nodal displacements are constants yields:

$$\Pi_p = \tfrac{1}{2}\{\mathbf{d}\}^{\mathrm{T}} \cdot \left(\int_A \left[\mathbf{N}^{\mathbf{RD}}\right]^{\mathrm{T}} [\mathbf{T}]^{\mathrm{T}} [\mathbf{k}][\mathbf{T}]\left[\mathbf{N}^{\mathbf{RD}}\right] dA \right) \cdot \{\mathbf{d}\} \qquad \text{Equation 7.18}$$

The element stiffness matrix is determined by minimizing the potential energy of the interface with respect to the nodal the displacements, which is achieved by differentiation with respect to $\{d\}$. The resulting stiffness matrix is given by:

$$\left[\mathbf{K}_{\mathbf{EL}}\right] = \int_A \left[\mathbf{N}^{\mathbf{RD}}\right]^{\mathrm{T}} [\mathbf{T}]^{\mathrm{T}} [\mathbf{k}][\mathbf{T}]\left[\mathbf{N}^{\mathbf{RD}}\right] dA \qquad \text{Equation 7.19}$$

where: $\left[\mathbf{K}_{\mathbf{EL}}\right]$ = the element stiffness matrix

The integral in Equation 7.19 is typically evaluated by some type of numerical integration, such as Gauss quadrature. Goodman et al. (1968) integrated the stiffness matrix equation exactly, but for more general problems, it is more convenient to use numerical procedures. Morrison (1995) showed that for plane strain interface elements based on Equation 7.19, Newton-Cotes integration is preferred over Gauss integration. For plane strain interface elements, the use of Newton-Cotes integration reduces or eliminates problems with oscillation of stresses in adjacent interface elements (Qui et al. 1991, Schellekens and De Borst 1993, Morrison 1995). As will be shown later, the use of Newton-Cotes integration for axisymmetric interface elements creates additional problems, and as a result, Gauss integration is still recommended for integrating axisymmetric interface elements.

The area of integration in Equation 7.19 is the contact area of the interface, which is not in the plane of the mesh for either plane strain or axisymmetric problems. Details of out-of-plane mapping relationships for both axisymmetric and plane strain formulations are provided in Appendix D. The out-of-plane area is mapped into the natural coordinate system using the following relationship:

$$\iint_A dA = \int_\varsigma \int_\xi \sqrt{\frac{\partial x}{\partial \xi}^2 + \frac{\partial y}{\partial \xi}^2}\, d\xi d\varsigma \qquad \text{Equation 7.20}$$

where: ξ = natural coordinate along the interface in the mesh
ς = natural coordinate perpendicular to the plane of the mesh

For plane strain analysis with a unit thickness (z = 1), Equation 7.20 reduces to:

$$\iint_A dA = \int_\xi \sqrt{\frac{\partial x}{\partial \xi}^2 + \frac{\partial y}{\partial \xi}^2}\, d\xi \qquad \text{Equation 7.21}$$

Equation 7.19 can now be integrated numerically, as all terms are functions of the shape functions or the derivatives of the shape functions with respect to the natural coordinates, which can all be evaluated directly at the integration points.

For axisymmetric analysis, Equation 7.20 reduces to:

$$\iint_A dA = 2\pi \int_\xi r \sqrt{\frac{\partial r}{\partial \xi}^2 + \frac{\partial z}{\partial \xi}^2}\, d\xi \qquad \text{Equation 7.22}$$

If the coordinate r is interpolated using the Lagrangian interpolation functions and the nodal coordinates, Equation 7.19 can be evaluated numerically for the axisymmetric case. It is important to note that in Equation 7.22, the radius r is not necessarily constant along the element, and therefore must remain in the integrand. This point is often misinterpreted, as it is tempting to multiply the stiffness matrix for plane strain analysis by a factor of $2\pi r$ to account for the

thickness of the element perpendicular to the plane of the mesh to get the stiffness matrix for axisymmetric analysis. This is incorrect, as can be seen from Equation 7.22. If the interface is oriented vertically, so that the radius does not vary along the interface, multiplying the plane strain stiffness matrix by $2\pi r$ will give the correct axisymmetric stiffness matrix. For all other cases, the stiffness matrix will be incorrect. The correct expression for the stiffness matrix for the axisymmetric, mapped, isoparametric interface element is:

$$\left[\mathbf{K}_{\mathbf{EL}}\right] = 2\pi \cdot \int_{-1}^{+1} \left[\mathbf{N}^{\mathbf{RD}}\right]^{\mathrm{T}} \left[\mathbf{T}\right]^{\mathrm{T}} \left[\mathbf{k}\right] \left[\mathbf{T}\right] \left[\mathbf{N}^{\mathbf{RD}}\right] \cdot \left(N_i r_i \sqrt{\left(\frac{\partial N_i}{\partial \xi} r_i\right)^2 + \left(\frac{\partial N_i}{\partial \xi} z_i\right)^2} \right) d\xi \qquad \text{Equation 7.23}$$

where: $\left[\mathbf{N}^{\mathbf{RD}}\right] = \begin{bmatrix} -N_1 & 0 & -N_2 & 0 & N_2 & 0 & N_1 & 0 \\ 0 & -N_1 & 0 & -N_2 & 0 & N_2 & 0 & N_1 \end{bmatrix}$

= interpolation function matrix for relative displacements

$\left[\mathbf{T}\right] = \dfrac{1}{\sqrt{\left(\frac{\partial N_i}{\partial \xi} \cdot r\right)^2 + \left(\frac{\partial N_i}{\partial \xi} \cdot z_i\right)^2}} \begin{bmatrix} \frac{\partial N_i}{\partial \xi} \cdot r_i & \frac{\partial N_i}{\partial \xi} \cdot z_i \\ -\frac{\partial N_i}{\partial \xi} \cdot z_i & \frac{\partial N_i}{\partial \xi} \cdot r_i \end{bmatrix}$

= the transformation matrix

$\left[\mathbf{k}\right]$ = the material property matrix

N_i = the interpolation functions

r_i = the r coordinate at node i

z_i = the z coordinate at node i

ξ = the natural coordinate along the interface

In Equation 7.23, the subscript indicates summation over the number of nodal pairs with identical coordinates.

In developing computer programs for finite element analysis, the practice of simply multiplying the plane strain stiffness matrix by $2\pi r$ should be avoided, and the element stiffness should be integrated correctly to avoid unexpected results as a consequence of inexact stiffness integration.

Problems with Newton-Cotes Integration for Axisymmetric Elements

As noted previously, the integral in Equation 7.23 is typically evaluated numerically using either Gauss quadrature or Newton-Cotes integration. The interpolation functions and the spatial derivatives of the interpolation functions with respect to the natural coordinates can be computed at each integration point, and the nodal coordinates are known constants for each element. For Newton-Cotes integration, the integration points are located at the nodal points. The locations of the integration points and values of the interpolation functions, integration weights, and derivatives with respect to natural coordinates for a linear interface using second order integration for both Gauss integration and Newton-Cotes integration are compared in Table 7.1.

Table 7.1 - Comparison of Integration Points for Gauss Integration and Newton-Cotes Integration

	Gauss Point 1	**Gauss Point 2**	**N-C Int. Pt. 1**	**N-C Int. Pt. 2**
ξ	-0.577350269189	0.577350269189	-1	1
Int. Wt.	1	1	1	1
N_1	0.788675134595	0.211324865406	1	0
N_2	0.211324865406	0.788675134595	0	1
$dN_1/d\xi$	-0.5	-0.5	-0.5	-0.5
$dN_2/d\xi$	0.5	0.5	0.5	0.5

Using Newton-Cotes integration, at any integration point the interpolation functions all have values of either 0 or 1. This, in effect, uncouples the nodes along the interface, so that the behavior of the interface is governed only by each pair of nodes with identical coordinates, and not by the other nodal pairs along the interface. Although the use of Newton-Cotes integration has been

shown to reduce stress oscillations in interface elements (Morrison 1995), problems can arise when using Newton-Cotes integration for axisymmetric analysis.

If a node connected to an interface is located along the axis r = 0, Newton-Cotes integration will provide erroneous results. This is best illustrated by considering an example of a linear interface element using Newton-Cotes integration. Equation 7.23, which defines the stiffness matrix for this element, can be expanded to obtain a more explicit form as follows:

$$\left[\mathbf{K}_{\mathbf{EL}}\right] = 2\pi\int_{-1}^{+1}\begin{bmatrix} N_1^{\,2}\left[\mathbf{TkT}\right] & N_1N_2\left[\mathbf{TkT}\right] & -N_1N_2\left[\mathbf{TkT}\right] & -N_1^{\,2}\left[\mathbf{TkT}\right] \\ N_1N_2\left[\mathbf{TkT}\right] & N_2^{\,2}\left[\mathbf{TkT}\right] & -N_2^{\,2}\left[\mathbf{TkT}\right] & -N_1N_2\left[\mathbf{TkT}\right] \\ -N_1N_2\left[\mathbf{TkT}\right] & -N_2^{\,2}\left[\mathbf{TkT}\right] & N_2^{\,2}\left[\mathbf{TkT}\right] & N_1N_2\left[\mathbf{TkT}\right] \\ -N_1^{\,2}\left[\mathbf{TkT}\right] & -N_1N_2\left[\mathbf{TkT}\right] & N_1N_2\left[\mathbf{TkT}\right] & N_1^{\,2}\left[\mathbf{TkT}\right] \end{bmatrix}$$
$$\cdot\left(\left(N_1r_1 + N_2r_2\right)\sqrt{\left(\frac{\partial N_1}{\partial\xi}r_1 + \frac{\partial N_2}{\partial\xi}r_2\right)^2 + \left(\frac{\partial N_1}{\partial\xi}z_1 + \frac{\partial N_2}{\partial\xi}z_2\right)^2}\right)\cdot d\xi$$

where: $\left[\mathbf{TkT}\right] = \left[\mathbf{T}\right]^{\mathrm{T}}\cdot\left[\mathbf{k}\right]\cdot\left[\mathbf{T}\right]$

Remembering that at node i the value of N_i is 1 and the value of all other interpolation functions is 0, the expression for the stiffness matrix for this element becomes:

$$\left[\mathbf{K}_{\mathbf{EL}}\right] = 2\pi\sum_{IP}\begin{bmatrix} N_1^{\,2}\left[\mathbf{TkT}\right] & 0 & 0 & -N_1^{\,2}\left[\mathbf{TkT}\right] \\ 0 & N_2^{\,2}\left[\mathbf{TkT}\right] & -N_2^{\,2}\left[\mathbf{TkT}\right] & 0 \\ 0 & -N_2^{\,2}\left[\mathbf{TkT}\right] & N_2^{\,2}\left[\mathbf{TkT}\right] & 0 \\ -N_1^{\,2}\left[\mathbf{TkT}\right] & 0 & 0 & N_1^{\,2}\left[\mathbf{TkT}\right] \end{bmatrix}$$
$$\cdot\left(N_1r_1 + N_2r_2\right)\sqrt{\left(\tfrac{\partial N_1}{\partial\xi}r_1 + \tfrac{\partial N_2}{\partial\xi}r_2\right)^2 + \left(\tfrac{\partial N_1}{\partial\xi}z_1 + \tfrac{\partial N_2}{\partial\xi}z_2\right)^2}\cdot\left(\text{Int. Wt.}\right)$$

Substituting values from Table 7.1 for the Newton-Cotes integration points yields:

$$\left[\mathbf{K}_{\mathbf{EL}}\right] = 2\pi\left(\frac{1}{2}\right)\cdot\sqrt{\left(r_2 - r_1\right)^2 + \left(z_2 - z_1\right)^2}$$
$$\cdot\left(\left(r_1\right)\begin{bmatrix} \left[\mathbf{TkT}\right] & 0 & 0 & -\left[\mathbf{TkT}\right] \\ 0 & 0 & 0 & 0 \\ 0 & 0 & 0 & 0 \\ -\left[\mathbf{TkT}\right] & 0 & 0 & \left[\mathbf{TkT}\right] \end{bmatrix} + \left(r_2\right)\begin{bmatrix} 0 & 0 & 0 & 0 \\ 0 & \left[\mathbf{TkT}\right] & -\left[\mathbf{TkT}\right] & 0 \\ 0 & -\left[\mathbf{TkT}\right] & \left[\mathbf{TkT}\right] & 0 \\ 0 & 0 & 0 & 0 \end{bmatrix}\right)$$

If either of the pairs of nodes defining the interface is located at $r = 0$, one of the two constituent matrices in the expression above does not contribute to the element stiffness matrix. The resulting zero stiffness terms, when assembled into the global stiffness matrix, result in no contribution from the interface element to the global stiffness between the two nodes where $r = 0$. Since this pair of nodes is not connected by any other elements in the structure, the nodes are unconnected in terms of global stiffness. As a result, there is no energy associated with the relative displacement of this pair of nodes, and the energy resulting from displacements at this pair of nodes is due only to strains in the adjacent two-dimensional elements. This situation would be analogous to defining a mesh of two-dimensional elements, but ignoring displacement compatibility at one node. In other words, there is neither displacement continuity across this pair of nodes with identical coordinates, nor is there any stiffness term controlling the relative displacement of the two nodes. When analyzing an axisymmetric problem, the radial displacements along the $r = 0$ line (the z-axis) are typically constrained ($u = 0$), so the zero stiffness terms have no effect on the radial displacements. If the interface is not oriented in the horizontal plane, however, the shear displacement is due in part to both the radial and vertical displacements, so the shear displacements are affected by the zero stiffness terms. In addition, the normal displacements and both the shear and normal stresses are affected by the zero stiffness terms, and the resulting solution will produce unexpected results.

In addition to the problems that arise if an interface is located with one pair of nodes at $r = 0$, problems can also occur due to the fact that the stress distribution along the element boundary between the interface element and the adjacent two dimensional element is not consistent with the stress distribution along the interface element. This is due to the fact that the two dimensional elements are integrated using Gauss quadrature, but the interface elements are integrated using Newton-Cotes integration. For a given stress distribution along the inter-element boundary, the equivalent nodal loads based on Gauss quadrature and the equivalent nodal loads based on Newton-Cotes integration are not the same. Stated another way, a given set of nodal loads for the nodes on the inter-element boundary will result in different stress distributions along the boundary depending on which type of numerical integration is used. In plane strain, the distributions are identical only if the stress distribution is uniform, and vary only slightly if the distribution is linear. In fact, this difference in the stress distribution may be partly responsible for the improved performance of the elements using Newton-Cotes integration. In axisymmetric analysis, however, even for a uniform stress distribution the equivalent nodal loads are not the same for both types of numerical integration, due to the radius term in the integrand of Equation 7.23. If the distribution is not linear, the difference due to the type of numerical integration is magnified, and unexpected interface behavior can result.

Owing to the problems mentioned, Gauss quadrature appears to be the better choice for the integration of axisymmetric interface elements. While Newton-Cotes integration may perform well for axisymmetric elements under certain conditions, it appears to be safer to use Gauss quadrature, at least until the performance of Newton-Cotes integration for a variety of axisymmetric conditions is thoroughly investigated.

Constitutive Model for Interface Behavior

The relationship between stresses and relative displacements suggested by Goodman et al. (1968) is shown in Equation 7.14. As noted previously, they assumed that the stiffness terms are constant, which implies linear stress-relative displacement behavior. The stiffness terms can also be modeled using a nonlinear relationship. Clough and Duncan (1969, 1971) proposed using a hyperbolic function to model the stress-relative displacement behavior of soil-concrete interfaces. The model is similar in form to the popular hyperbolic model for stress-strain modeling of soils described by Duncan et al. (1980). Morrison (1995) describes the implementation of the hyperbolic model for interface behavior in detail. It should be noted that by properly adjusting the input parameters for the model, linearly elastic, or bilinear elastic behavior can be modeled in addition to the stress-dependent nonlinear behavior.

Description of Analyses Performed

The triaxial test specimen and end platen were modeled using 4-node isoparametric quadrilateral elements with linear interpolation. The interface between the end platen and the specimen was modeled using the previously described interface elements. Since the specimen is symmetric about its axis as well as a plane perpendicular to its axis at the mid-height, the specimen can be adequately modeled using a planar mesh that extends from the mid-height to the upper end and from the axis to the perimetric surface. The mesh and boundary conditions used to simulate the triaxial test specimen, interface, and end platen are shown in Figure 7.1. The mesh contains 392 soil elements representing a specimen with a 2.8-inch diameter and a 5.6-inch height. Axial displacements were prescribed along the top surface of the end platen in order to load the specimen.

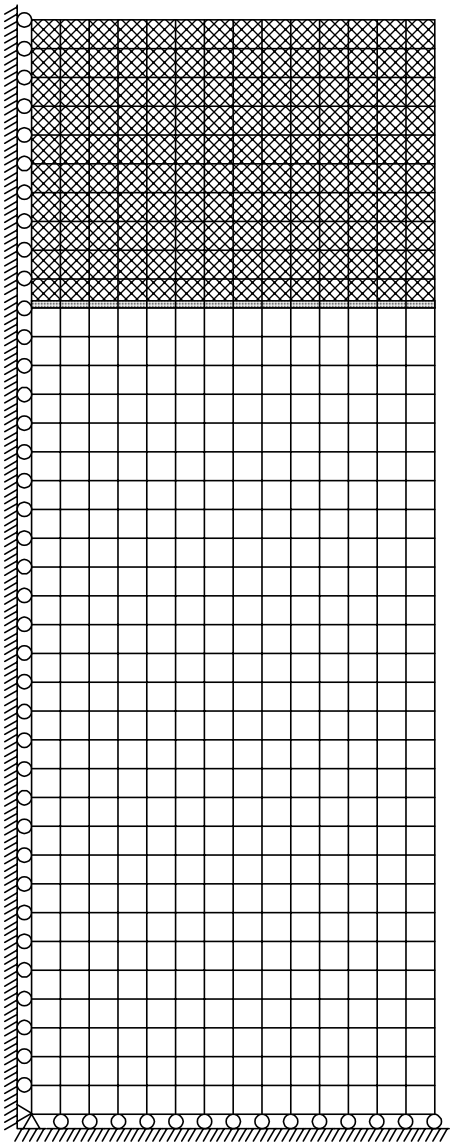

Figure 7.1 - Finite Element Mesh Used to Model a Triaxial Test Specimen With L/D = 2

Prior to investigating varying degrees of end friction, the effects of complete end restraint were evaluated for cylinders with L/D ratios of 1 and 2. These analyses were accomplished by pinning the nodes along the top surface of the specimen against displacement in the radial direction and prescribing axial displacements at these nodes. Since complete end restraint results in the most

significant effects due to end conditions, both the modulus of elasticity and Poisson's ratio were varied in order to evaluate their influence on measured stress-strain response and variations in stress within the specimen. The analyses for an L/D ratio of 1 facilitated comparison with the analytical solutions previously discussed, as well as provided a baseline for evaluating the effects of increasing the L/D ratio. For L/D = 1, a 20-element by 20-element mesh was used, and for L/D = 2, the mesh in Figure 7.1, but without the platen and interface, was used.

In addition to the analyses of complete end restraint, the interface elements described previously were used to model varying degrees of end restraint for specimens with a value of L/D of 2. Two interface conditions, representing conventional end platen behavior and lubricated end platen behavior, were generally modeled. The required material parameters were determined based on the results of interface direct shear tests described in Chapter 6. A summary of the parameters used for the analyses is shown in Table 7.2.

Table 7.2 - Interface Properties Used in Finite Element Analyses

	Free Ends (ϕ_{int} = 0°)	Lubr. Ends (ϕ_{int} = 0.8°)	Conv. Ends (ϕ_{int} = 28.5°)
Cohesion, c (psi)	0.0	0.0	0.0
Friction Angle, ϕ (deg)	0.0	0.8	28.5
Tensile Strength, σ_t (psi)	0.0	0.0	0.0
Reduction Factor, R_f	0.0	0.0	0.0
Initial Shear Stiffness Coefficient, k_j	0.0	120	5000
Exponent, n	0.0	1.00	0.90
Compressive Stiffness, k_{nc} (psi)	10^9	10^9	10^9
Tensile Stiffness, k_{nt} (psi)	10^9	10^9	10^9
Failure Shear Stiffness, k_{sf} (psi)	0.0	0.0	0.0

Analyses using linear elastic material models were conducted to facilitate comparison with the conditions of complete restraint and complete slip at the interface, and to evaluate the variations in stresses that develop in partially restrained specimens during compression. Although linear elasticity is well suited for performing parametric studies and relative comparisons, its applicability to soils, particularly at other than very small strain levels, is limited. To better represent conditions after failure, analyses were performed using the Drucker-Prager elasto-plastic model. The Drucker-Prager model uses linear elasticity to represent behavior prior to yield, and perfect plasticity to represent behavior after yield (Desai and Siriwardane 1984, Chen and Mizuno 1990, Zienkiewicz and Taylor 1991). The yield surface can be described by:

$$F = \alpha \cdot J_1 + K$$ Equation 7.24

where: J_1 = first stress invariant
α = constant
K = constant

The yield criterion is based on the second deviatorical stress invariant and the yield surface as follows:

$$\sqrt{J_{2D}} - \alpha \cdot J_1 - K = 0$$ Equation 7.25

where: J_{2D} = second deviatorical stress invariant

If the state of stress lies within the yield surface, elastic behavior occurs, and if the state of stress is on the yield surface (when the yield criterion is met), elastic and plastic behavior occur. Since triaxial test results are typically interpreted based on the Mohr-Coulomb failure criterion, which does not account for the intermediate principal stress, the Drucker-Prager failure surface was matched to the Mohr-Coulomb criterion for the case of triaxial compression, when $\sigma_1 > \sigma_2 = \sigma_3$ (Chen and Mizuno 1990). The resulting expressions for the two constants are:

$$\alpha = \frac{2 \cdot \sin\phi}{\sqrt{3} \cdot (3 - \sin\phi)}$$ Equation 7.26

$$K = \frac{6 \cdot c \cdot \cos\phi}{\sqrt{3} \cdot (3 - \sin\phi)}$$ Equation 7.27

where: c = cohesion intercept
ϕ = angle of internal friction

It is well known that the classical Drucker-Prager model results in excessive dilation once plastic strains occur (Desai and Siriwardane 1984, Chen and Mizuno 1990, Morrison 1995). In order to preserve the condition of zero volume change after yielding, the classical model was modified so that the

plastic potential surface did not vary with mean normal stress. This modification results in an unsymmetrical stiffness matrix, which the solver employed in SAGE is capable of handling, and preserves the zero volume change condition during plastic yielding.

Results of Finite Element Analyses

Linear Elastic Cylinder

For linear elastic behavior of a cylinder, compression between completely frictionless ends will result in uniform states of stress and strain throughout the specimen. The radial and circumferential stresses will be equal to the applied external pressure at all strain levels, and the axial stress initially will be equal to the applied external pressure, but will increase with strain level. The states of stress and strain within the specimen can be summarized as follows:

$$\sigma_r = \sigma_\theta = \sigma_{cell} \qquad \varepsilon_r = \varepsilon_\theta = -\nu \cdot \varepsilon_a$$
$$\sigma_z = \sigma_{cell} + E \cdot \varepsilon_a \qquad \varepsilon_z = \varepsilon_a$$

Analyses were performed on cylinders with restrained ends for L/D ratios of 1 and 2 and varying values of Poisson's ratio in order to evaluate the influence of L/D ratio and Poisson's ratio on the measured response and distributions of stress within the cylinder.

Pinned End (L/D = 1)

Figure 7.2 shows the *measured* stress-strain behavior, defined by the total axial force and the cross-sectional area, and the *correct* stress-strain behavior, defined by triaxial loading with no end restraint, for a single value of Poisson's ratio. For the unconfined case, when the cell pressure is equal to zero, the correct stress-strain response is simply the well-known uniaxial stress-strain relationship. In the upper right panel of Figure 7.2, the plots for both values of

elastic modulus are identical, indicating that the apparent increase in stress due to end restraint can be normalized by the modulus for linear elastic behavior. The lower left panel demonstrates that the effect, in terms of the ratio of measured to correct stress, is independent of strain level. The lower right panel demonstrates that a single value of the ratio of measured stress to correct stress applies to the particular specimen shape, boundary conditions, and value of Poisson's ratio, irrespective of strain level or elastic modulus. Figure 7.3 shows the same relationships for a single value of elastic modulus and different values of Poisson's ratio. Again, the ratio of measured stress to correct stress is constant regardless of modulus and strain level, but varies with Poisson's ratio. For a value of Poisson's ratio of zero, the ratio would be unity, since there would be no tendency for lateral expansion of the specimen, and hence no end restraint effects. The maximum influence occurs for a value of Poisson's ratio of one half, at which the measured stress is approximately 25 percent greater than the correct stress. As demonstrated by the intermediate values plotted in Figure 7.3, the relationship between the apparent increase in stress and Poisson's ratio is not linear.

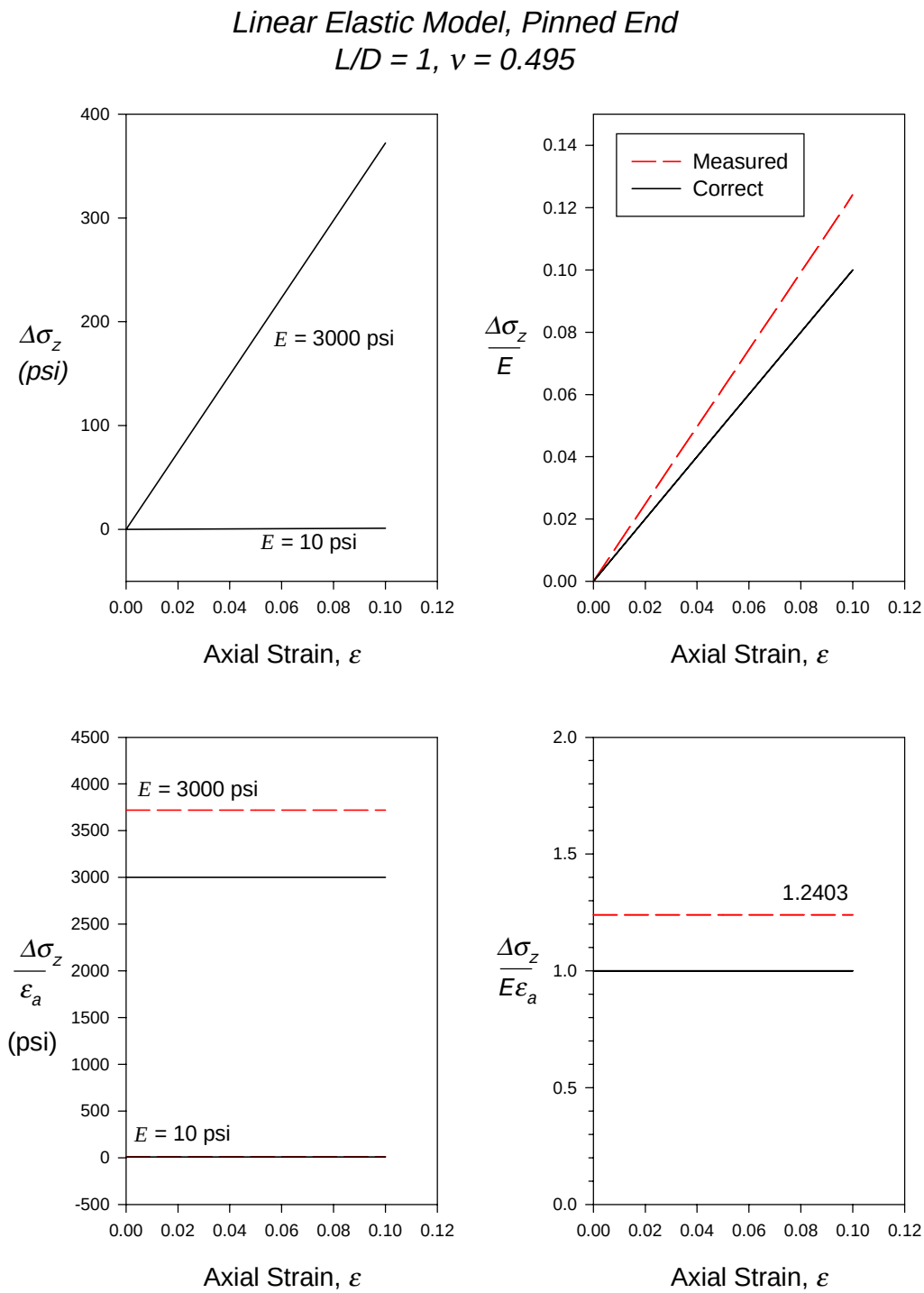

Figure 7.2 - Influence of Elastic Modulus on Measured Stress-Strain Response for L/D = 1

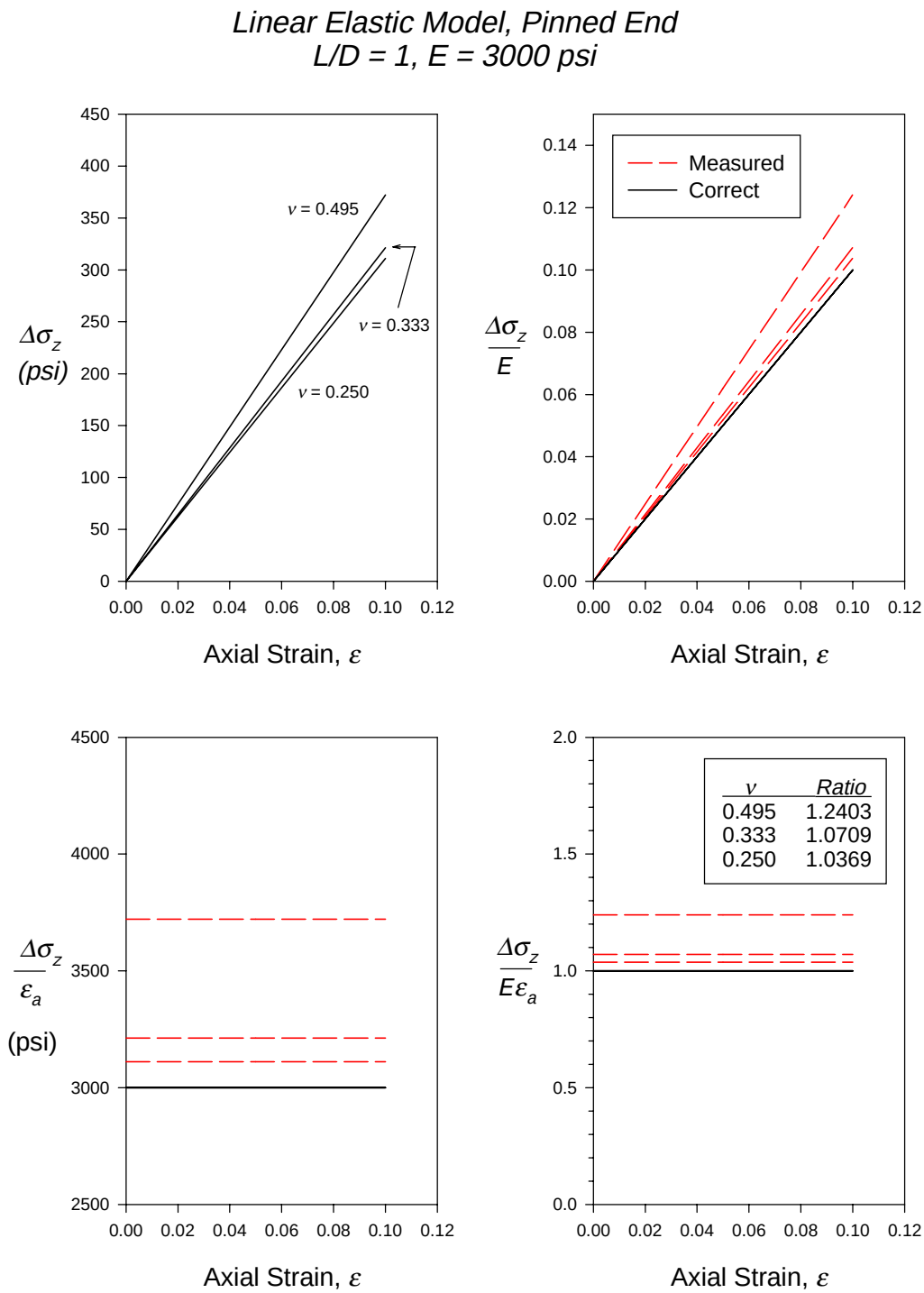

Figure 7.3 - Influence of Poisson's Ratio on Measured Stress-Strain Response for L/D = 1

Another consequence of end restraint is that the stresses within the specimen are not uniform. For frictionless ends, the radial and circumferential stresses are equal and uniform throughout the specimen, and the axial stress is uniform throughout the specimen. The confining stress or minor principal stress is equal to the radial stress, and the deviator stress is equal to the difference in axial stress and radial stress.

The variations in the two lateral stresses within the specimen at strain levels of 5 percent and 10 percent are shown in Figure 7.4. Since the *correct* lateral stresses are zero everywhere, Figure 7.4 demonstrates that the end restraint dramatically increases the lateral stresses in the specimen. The effect is the greatest near the ends, as would be anticipated, but the entire length of the specimen is affected, at least near the axis. The pattern of variation does not appear to be a function of strain level, but the magnitude of the variation is, and increases as strain level increases. Figure 7.4 also shows that the radial and circumferential stresses are not equal everywhere, as is assumed when interpreting triaxial test data.

Figure 7.5 shows the variations in axial stress and shear stress in the r-z plane. The *correct* axial stresses are 150 psi and 300 psi for axial strain levels of 5 percent and 10 percent, respectively. The *correct* shear stress in the r-z plane is zero at all locations. Again, the patterns of variation are similar at both strain levels, but the magnitude increases with strain. The axial stress is greater than the *correct* stress everywhere, and is not uniform on cross-sectional planes. At the specimen end, the axial stress is greatest at the perimeter of the specimen, while away from the ends, the stress is greatest at the axis. The shear stress in the plane of the mesh is greatest at the intersection of the perimetric surface and the specimen end and is only equal to zero in small regions of the specimen.

The variations in the deviator stress and the confining stress within the specimen at strain levels of 5 percent and 10 percent are shown in Figure 7.6. The *correct* deviator stress is equal to the *correct* axial stress, and the *correct* confining stress is equal to zero everywhere. The deviator stress varies significantly within the specimen, but is not always greater than the *correct* stress, as the axial stress is. This is because the increase in lateral stresses significantly increases the confining stress, particularly near the ends. The maximum value of confining stress occurs at the intersection of the axis and the specimen end, and is actually nearer to the value of *correct* deviator stress than *correct* confining stress. The minimum value of confining stress occurs at the mid-height of the specimen at the perimeter and has a negative value, indicating tension, for the unconfined loading case. The deviator stress has a maximum value at the mid-height of the specimen at the axis and a minimum value at the intersection of the specimen end and the axis. Figure 7.6 demonstrates that in the region near the specimen ends and along the axis, the confining stress is significantly increased and the deviator stress is significantly decreased due to end restraint. As a result, the material in this region is much stronger, and does not fail when predicted based on the average stresses calculated based on externally measured forces and displacements.

Linear Elastic Model, Pinned End

E = 3000 psi, ν = 0.495

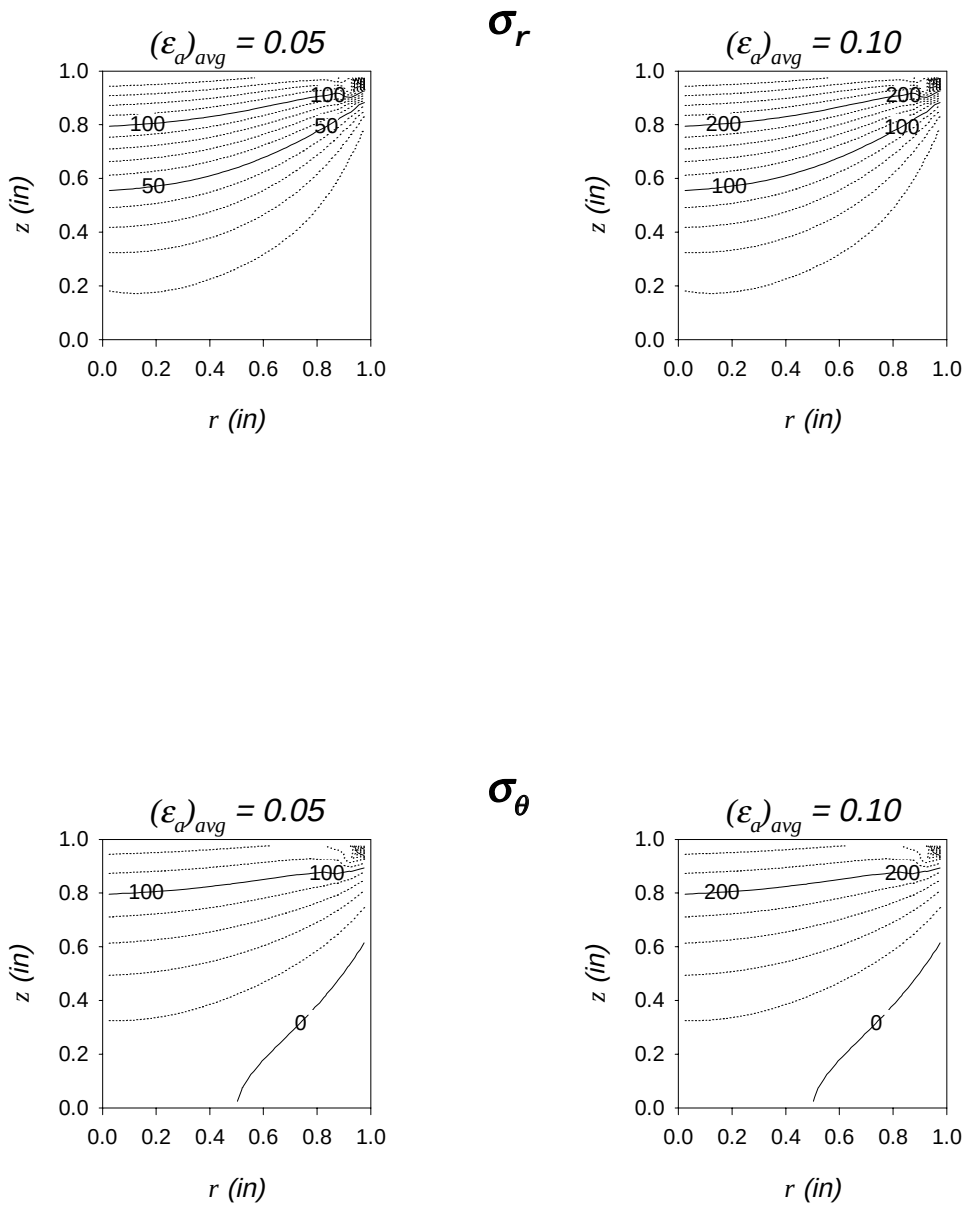

Figure 7.4 - Variation of Lateral Stresses for L/D = 1

Linear Elastic Model, Pinned End

E = 3000 psi, ν = 0.495

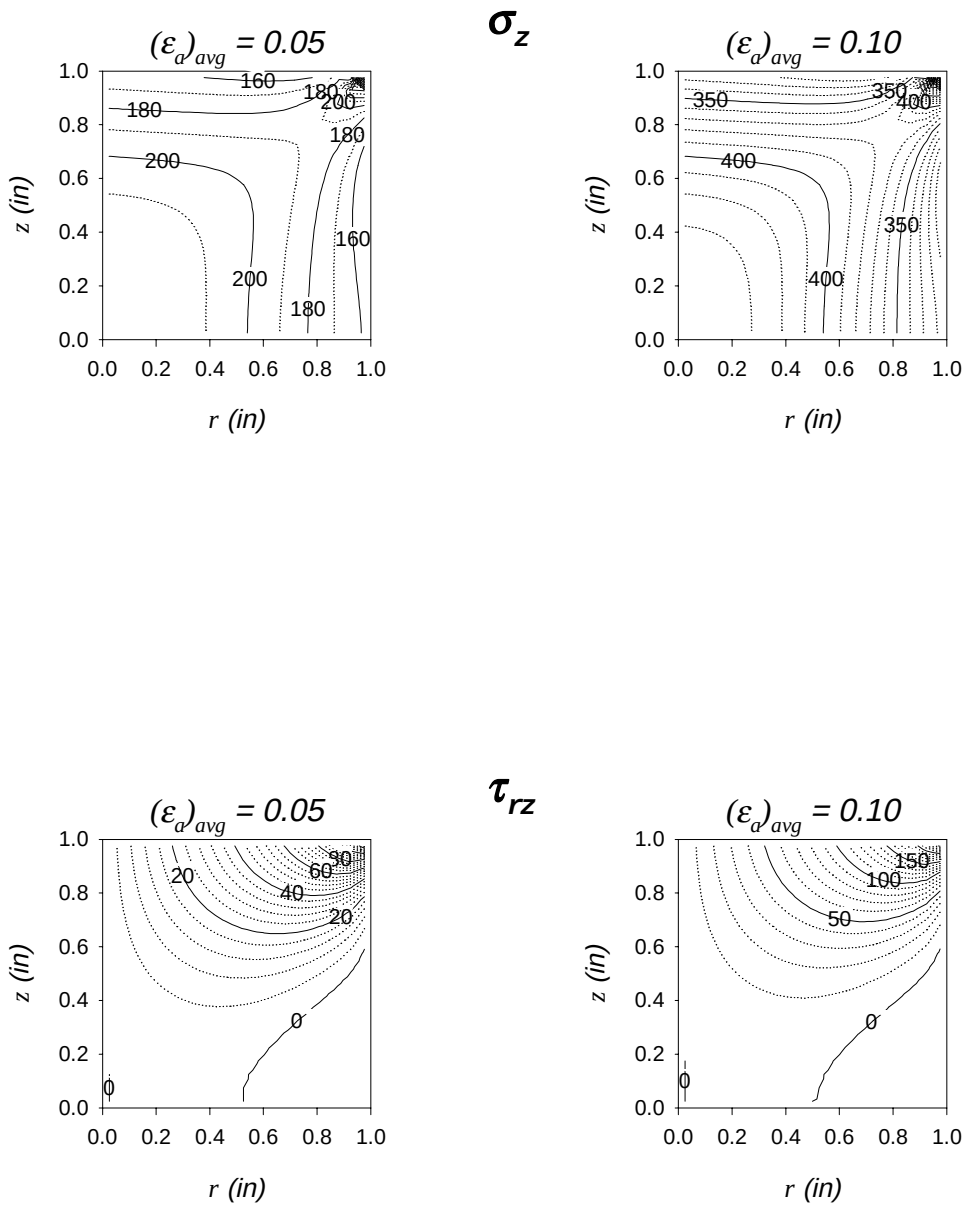

Figure 7.5 - Variation of Axial and Shear Stresses for L/D = 1

Linear Elastic Model, Pinned End

E = 3000 psi, ν = 0.495

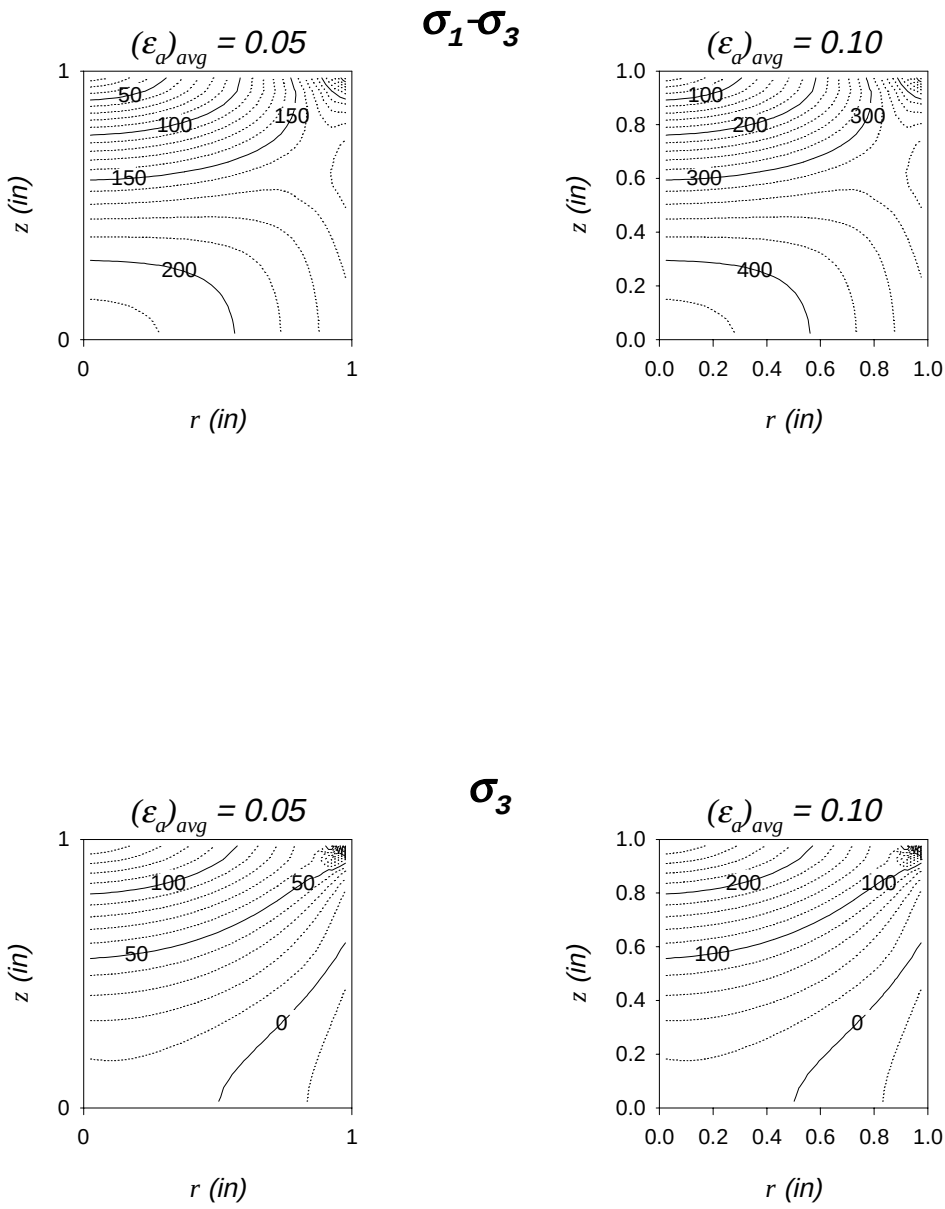

Figure 7.6 - Variation of Deviator and Confining Stresses for L/D = 1

Pinned End (L/D = 2)

In order to simulate more nearly typical conditions in the triaxial test, a hydrostatic pressure of 50 psi was applied prior to axial loading for the models with values of L/D of 2. The specimen radius for these models was 1.4 inches and the specimen height was 5.6 inches. If the material properties are identical, the value of L/D will have no effect on the stresses for frictionless ends. In other words, the stresses should be identical in cylinders with different L/D ratios at the same strain level.

Figure 7.7 shows the *measured* stress-strain behavior, defined by the total axial force and the cross-sectional area, and the *correct* stress-strain behavior, defined by triaxial loading with no end restraint, for a single value of Poisson's ratio. The upper right panel of Figure 7.7 shows that the apparent increase in stress due to end restraint can be normalized by the modulus for linear elastic behavior. The lower left panel demonstrates that the effect, in terms of the ratio of measured to correct stress, is independent of strain level. The lower right panel demonstrates that a single value of the ratio of measured stress to correct stress applies to the particular specimen shape, boundary conditions, and value of Poisson's ratio, irrespective of strain level or elastic modulus. Figure 7.8 shows the same relationships for a single value of elastic modulus and different values of Poisson's ratio. Again, the ratio of measured stress to correct stress is constant regardless of modulus and strain level, but varies with Poisson's ratio. For a value of Poisson's ratio of zero, the ratio would be unity, since there would be no tendency for lateral expansion of the specimen, and hence no end restraint effects. The maximum influence occurs for a value of Poisson's ratio of one half, at which the measured stress is approximately 12 percent greater than the correct stress. This apparent increase is approximately half of that predicted for L/D = 1. As demonstrated by the intermediate values plotted in Figure 7.8, the relationship between the apparent increase in stress and Poisson's ratio is not linear.

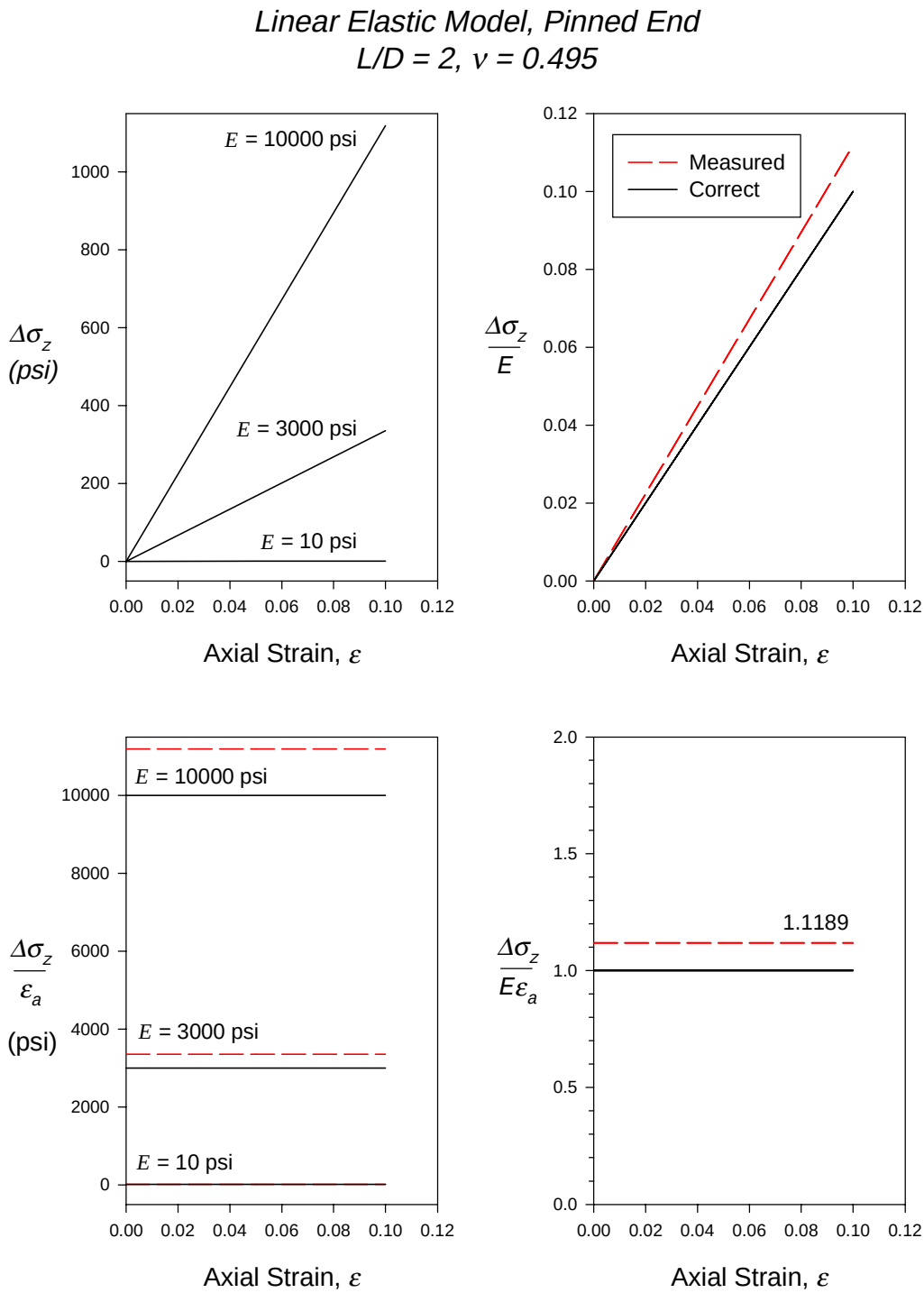

Figure 7.7 - Influence of Elastic Modulus on Measured Stress-Strain Response for L/D = 2

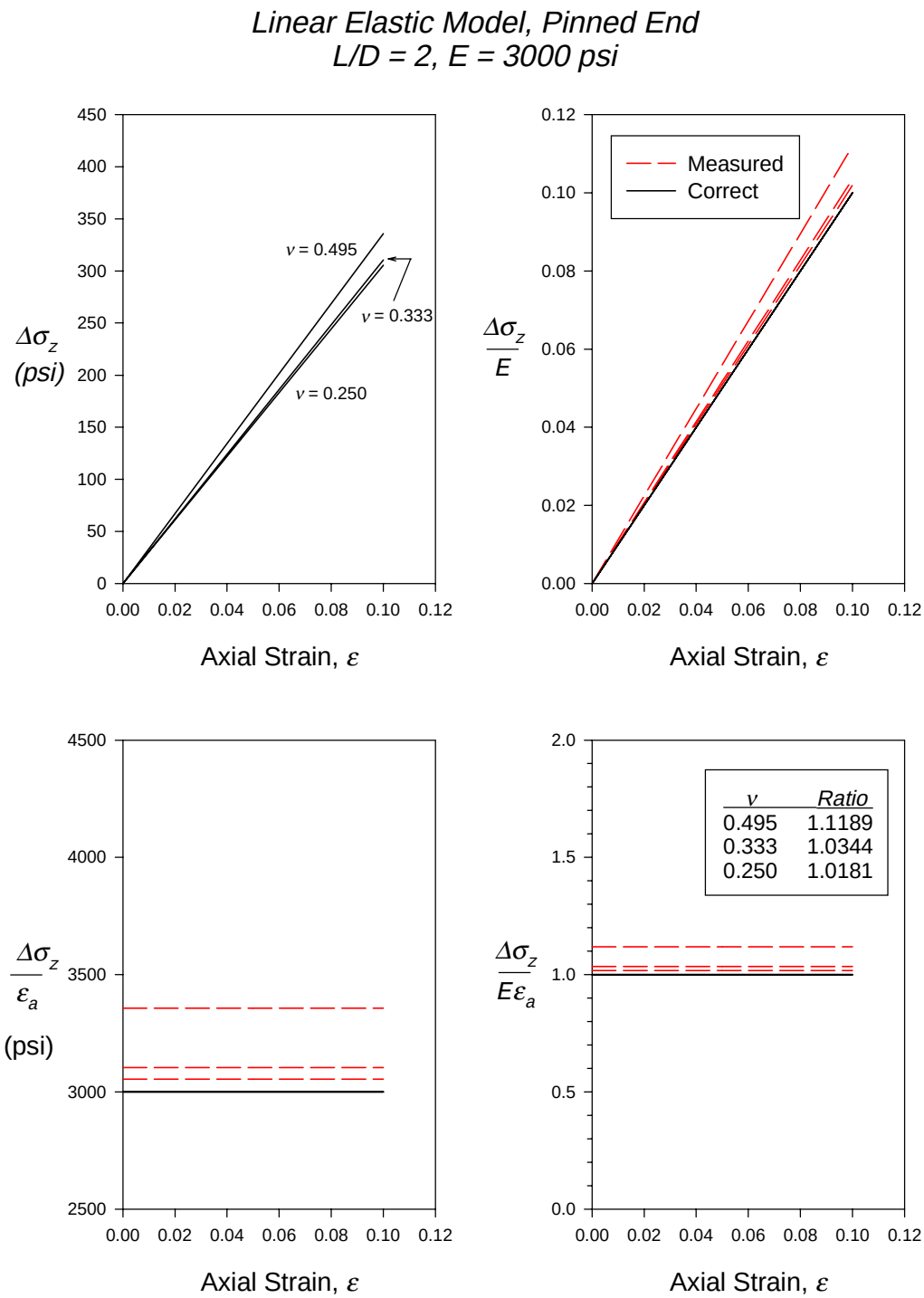

Figure 7.8 - Influence of Poisson's Ratio on Measured Stress-Strain Response for L/D = 2

The variations in the two lateral stresses within the specimen at strain levels of 5 percent and 10 percent are shown in Figure 7.9. Since the *correct* lateral stresses are equal to 50 psi everywhere, Figure 7.9 demonstrates that the end restraint dramatically increases the lateral stresses in the specimen near the ends. Near the mid-height and the axis, however, the lateral stresses are relatively unaffected by the end restraint, in contrast to the L/D = 1 case. Again, the pattern of variation does not appear to be a function of strain level, but the magnitude of the variation is dependent on the strain level and increases as strain level increases. Figure 7.9 also shows that the radial and circumferential stresses are not equal everywhere, as is assumed when interpreting triaxial test data, and that the end restraint appears to affect the radial stress more so than the circumferential stress.

Figure 7.10 shows the variations in axial stress and shear stress in the r-z plane. The *correct* axial stresses are 200 psi and 350 psi for axial strain levels of 5 percent and 10 percent, respectively. The *correct* shear stress in the r-z plane is zero everywhere. Again, the patterns of variation are similar at both strain levels, but the magnitude increases with strain. The axial stress is greater than the *correct* stress everywhere, and is not uniform on cross-sectional planes. At the specimen end, the axial stress is greatest at the perimeter of the specimen, while away from the ends, the stress is greatest at the axis. The shear stress in the plane of the mesh is greatest at the intersection of the perimetric surface and the specimen end, but is equal to zero in a significant portion of the specimen away from the ends.

The variations in the deviator stress and the confining stress within the specimen at strain levels of 5 percent and 10 percent are shown in Figure 7.11. The *correct* deviator stress is equal to the difference in the *correct* axial stress and the *correct* confining stress, or 150 psi and 300 psi, respectively, for axial strain levels of 5 percent and 10 percent. The *correct* confining stress is equal

to 50 psi everywhere. The deviator stress varies significantly within the specimen, but is not always greater than the *correct* stress, as the axial stress is. This is because the increase in lateral stresses significantly increases the confining stress, particularly near the ends. The deviator stress has a minimum value at the intersection of the specimen end and the axis. The maximum value of confining stress occurs at the intersection of the axis and the specimen end, and is actually nearer to the value of *correct* deviator stress than *correct* confining stress. The confining stress appears to be unaffected by the end restraint in a significant portion of the specimen away from the ends. Figure 7.11 demonstrates that in the region near the specimen ends and along the axis, the confining stress is significantly increased and the deviator stress is significantly decreased due to end restraint. As a result, the material in this region is much stronger, and does not fail when predicted based on the average stresses calculated based on externally measured forces and displacements.

Linear Elastic Model, Pinned End

E = 3000 psi, ν = 0.495

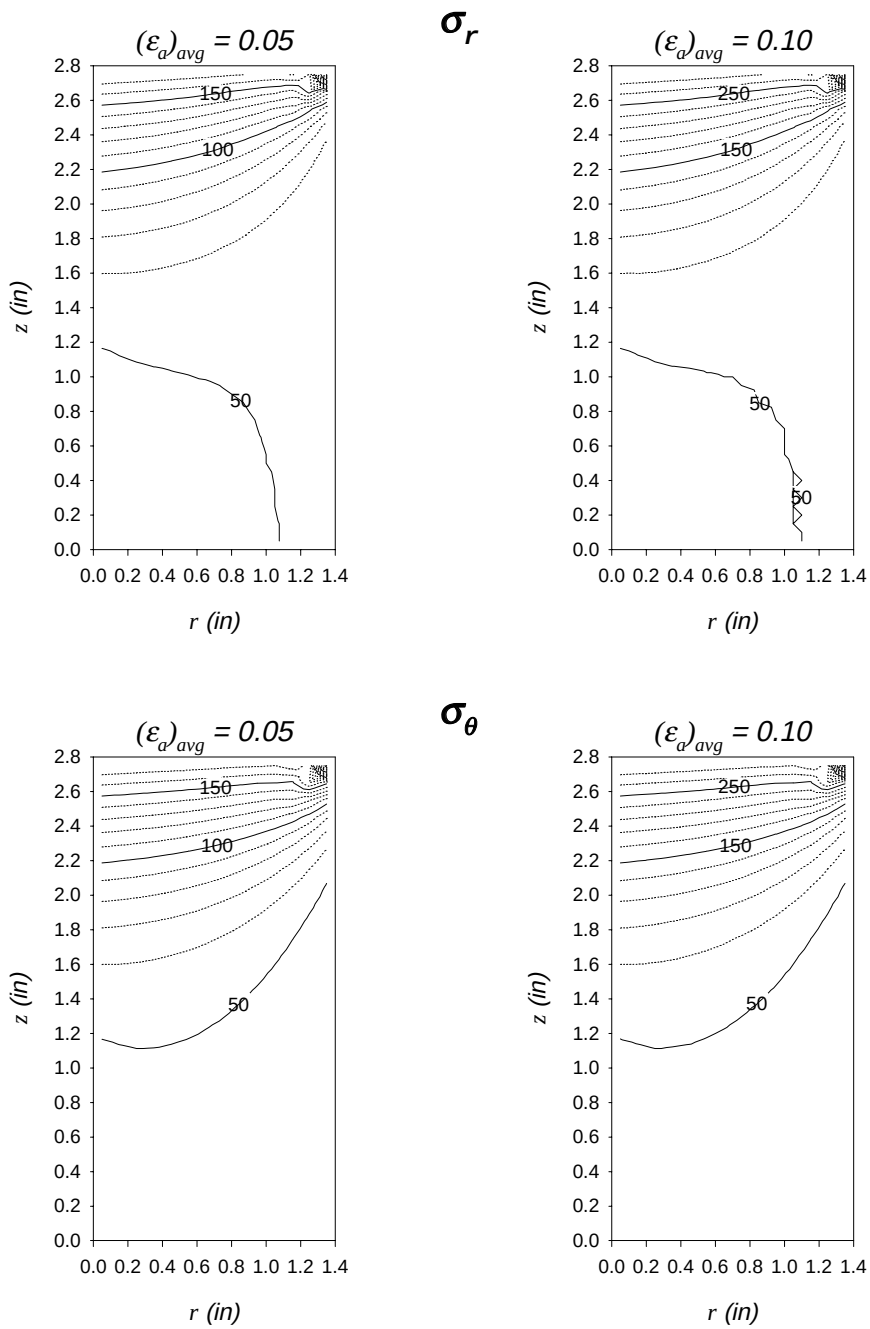

Figure 7.9 - Variation of Lateral Stresses for L/D = 2

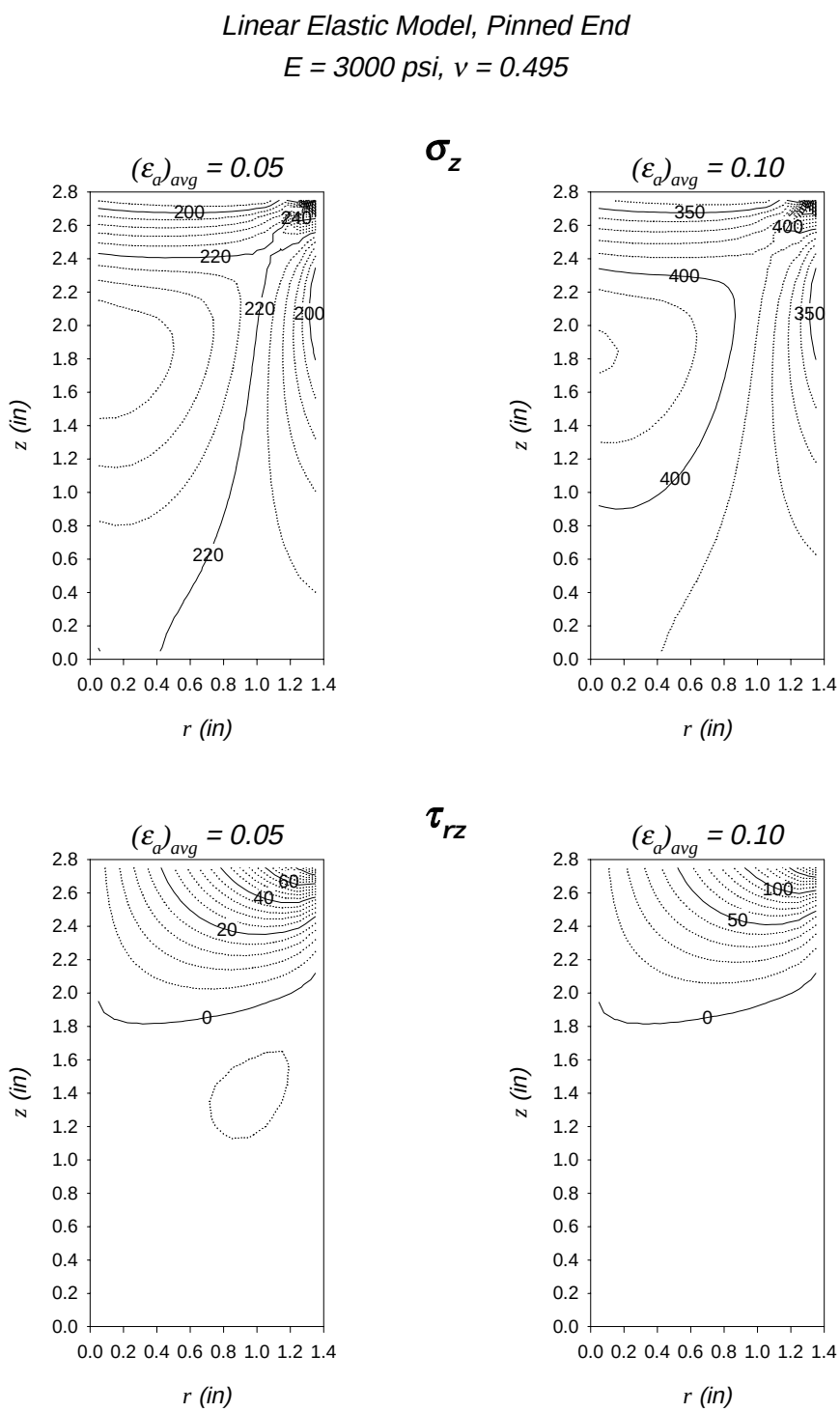

Figure 7.10 - Variation of Axial and Shear Stresses for L/D = 2

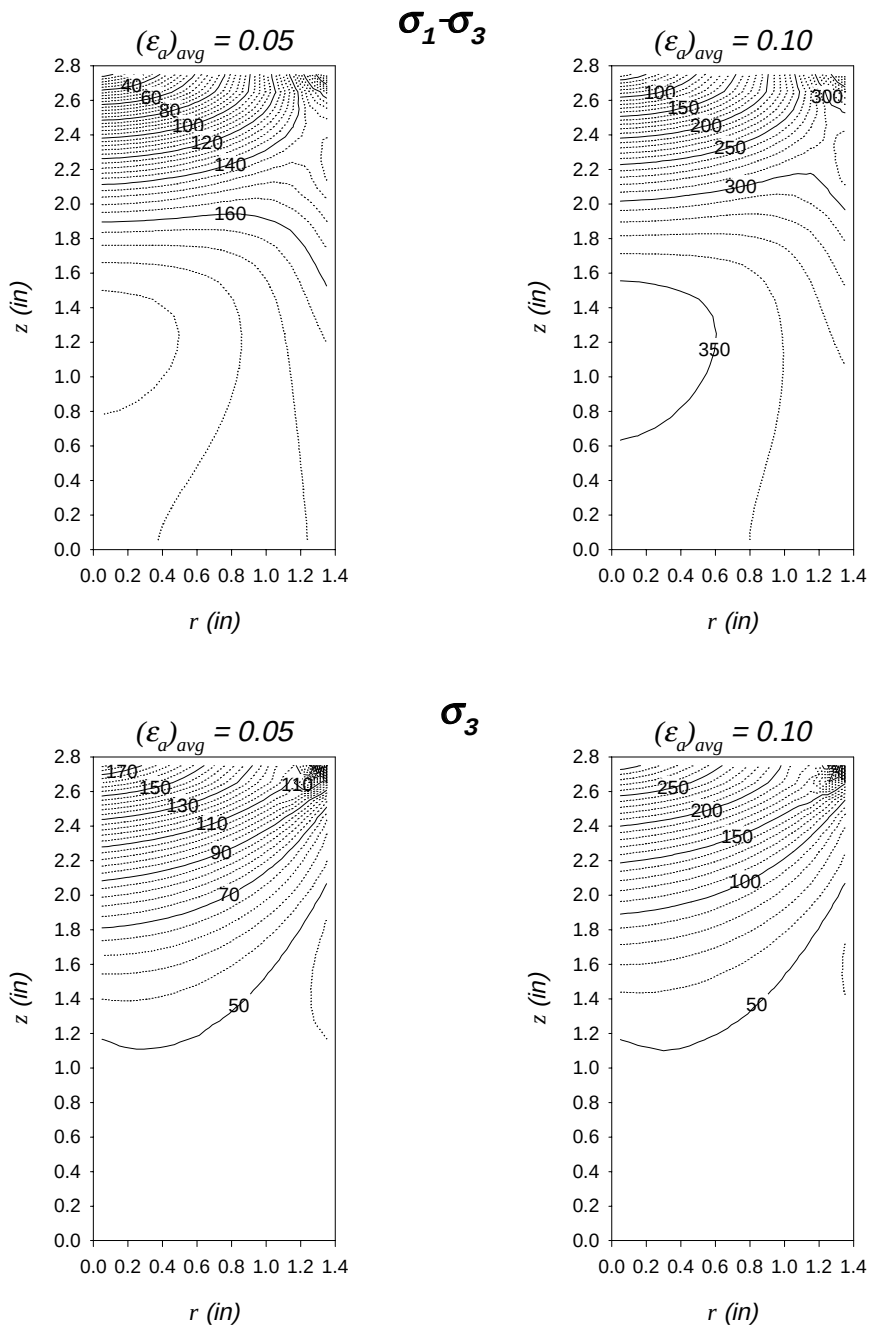

Figure 7.11 - Variation of Deviator and Confining Stresses for L/D = 2

The L/D = 2 case was analyzed with varying degrees of end friction in addition to the complete restraint condition. Figure 7.12 and Figure 7.13 show the measured stress-strain response for values of Poisson's ratio equal to 0.495 and 0.25, respectively. These figures demonstrate that for an interface friction angle of 28.5 degrees, the end friction results in an apparent increase in measured stress, but the effect is much less significant than for complete restraint. For an interface friction angle of 0.8 degrees, the effect of the end friction on the measured stress is negligible. Figure 7.12 and Figure 7.13 also demonstrate that for intermediate degrees of end restraint, the ratio of measured stress to correct stress is not constant with strain as is the case for complete restraint.

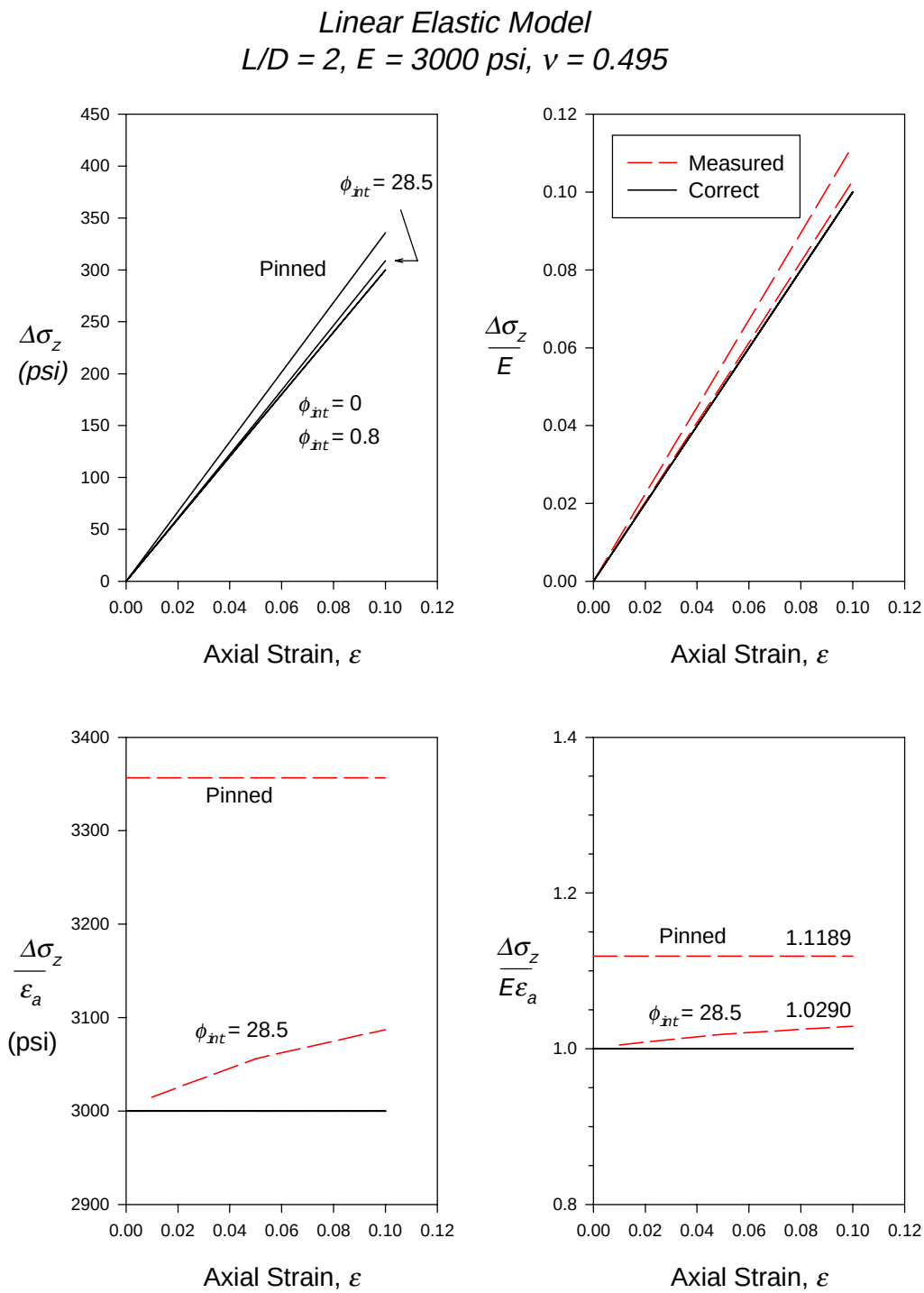

Figure 7.12 - Influence of End Restraint on Measured Stress-Strain Response for $\nu = 0.495$

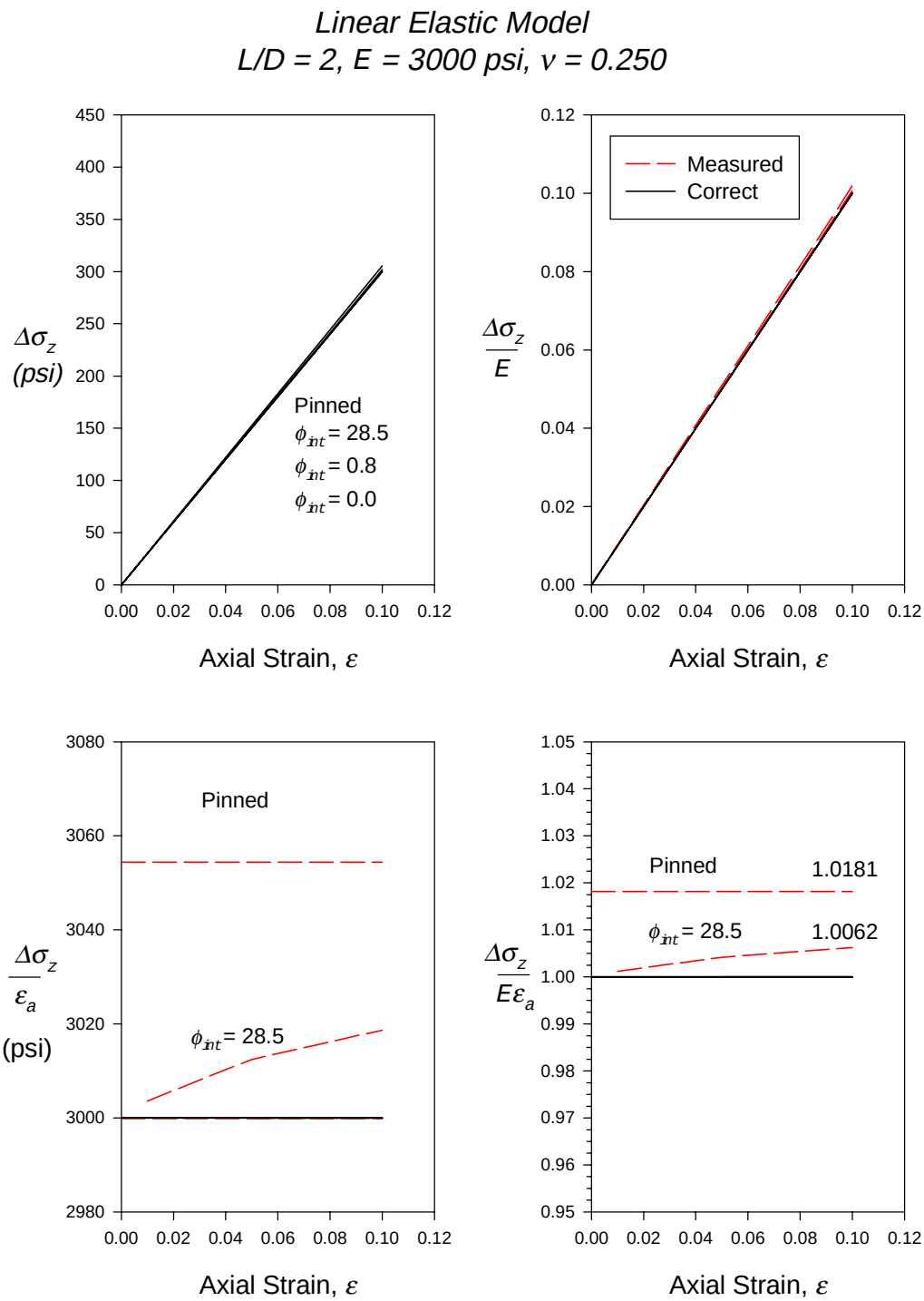

Figure 7.13 - Influence of End Restraint on Measured Stress-Strain Response for $\nu = 0.250$

Conventional End Condition (ϕ_{int} = 28.5°)

Figure 7.14, Figure 7.15, and Figure 7.16 show the lateral, axial, shear, deviator, and confining stress distributions at axial strain levels of 5 percent and 10 percent for an interface friction angle of 28.5 degrees. The general observations about the patterns of variation for the pinned end condition are valid for the cases with intermediate degrees of restraint as well. For this case, the magnitudes of the variation in the lateral stresses and the confining stress are approximately half of those for the pinned end case. The magnitudes of variation of the axial stress, shear stress, and deviator stress, although still significant, are reduced by more than half compared to the pinned end case. Figure 7.17 shows the normal and shear stresses on the interface elements, as well as the stress level, which is defined as the ratio of shear stress to shear strength based on the normal stress on the interface, for the ϕ_{int} = 28.5° condition. The lower panel shows that the interface elements are not near failure at an axial strain level of 10 percent.

Lubricated End Condition (ϕ_{int} = 0.8°)

Figure 7.18, Figure 7.19, and Figure 7.20 show the lateral, axial, shear, deviator, and confining stress distributions at axial strain levels of 5 percent and 10 percent for an interface friction angle of 0.8 degrees. Again, the general observations about the patterns of variation for the pinned end condition are valid. For this case, the variations in the lateral stresses and the confining stress appear to be negligible, with maximum values of approximately only 3 percent at an axial strain level of 10 percent. The magnitudes of variation of the axial stress and deviator stress also appear to be negligible, with values much less than 1 percent at an axial strain level of 10 percent. Figure 7.21 shows the normal and shear stresses on the interface elements and the stress level for the ϕ_{int} = 0.8° condition. The lower panel shows that the interface elements are not near failure at an axial strain level of 10 percent.

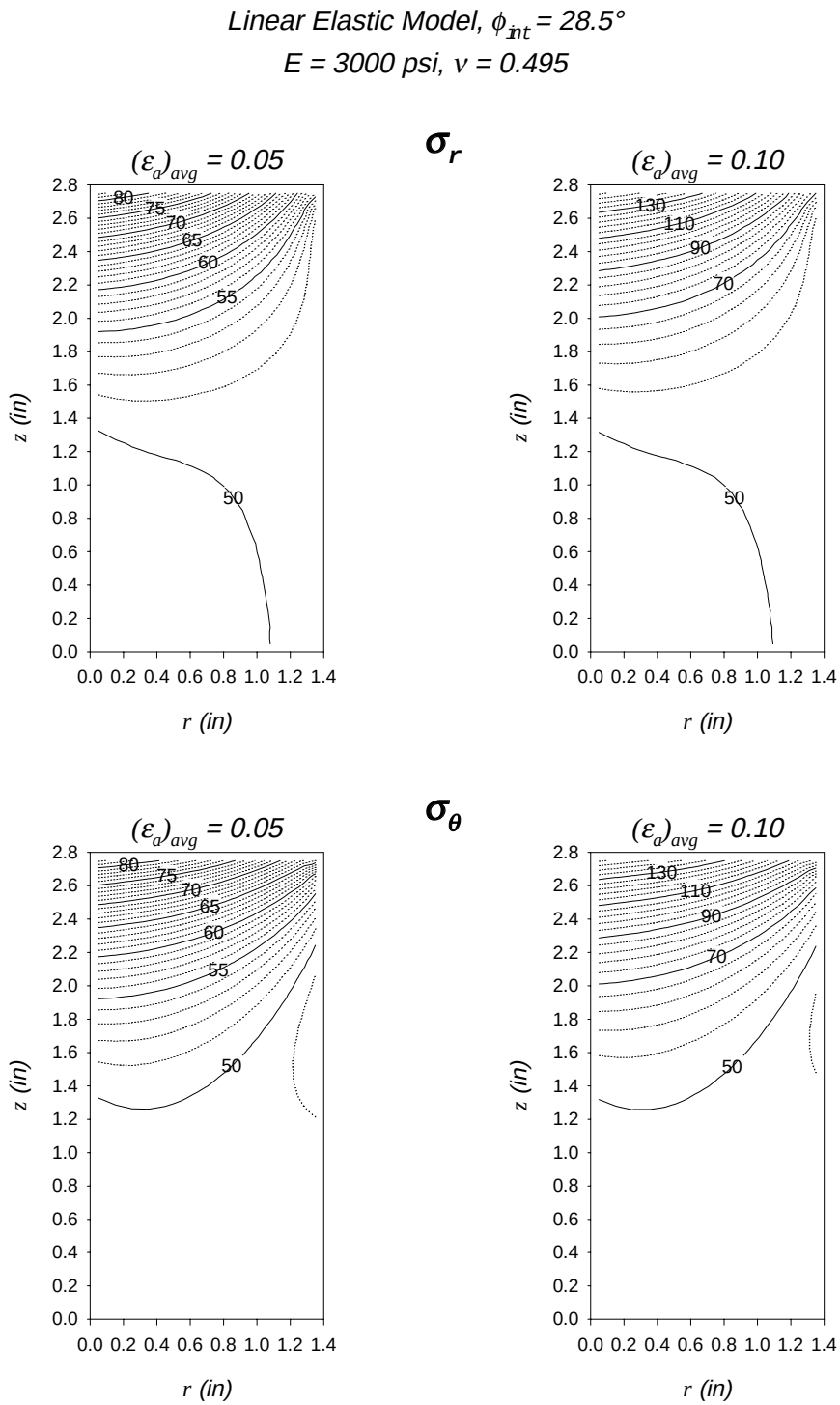

Figure 7.14 - Variation of Lateral Stresses for ϕ_{int} = 28.5°

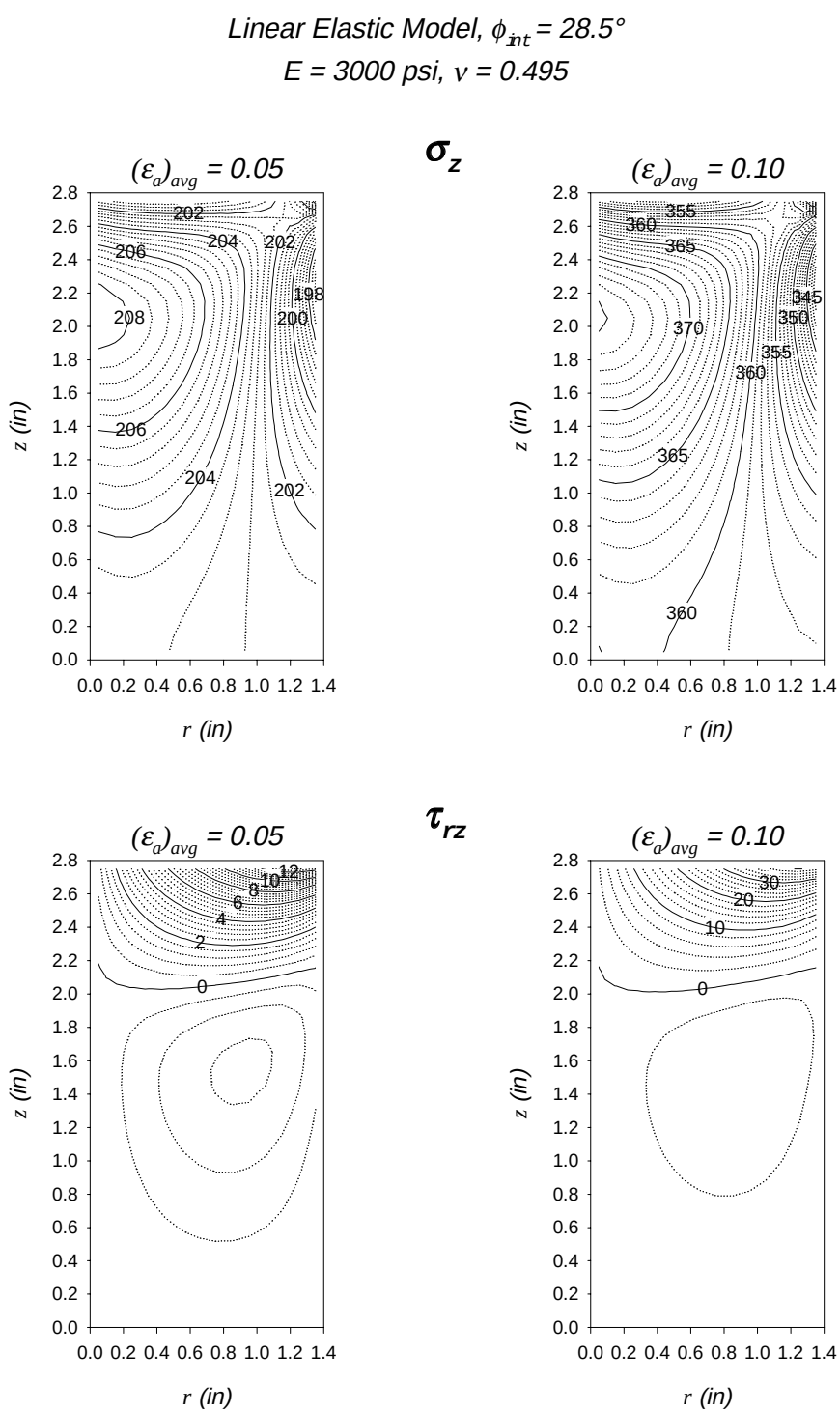

Figure 7.15 - Variation of Axial and Shear Stresses for ϕ_{int} = 28.5°

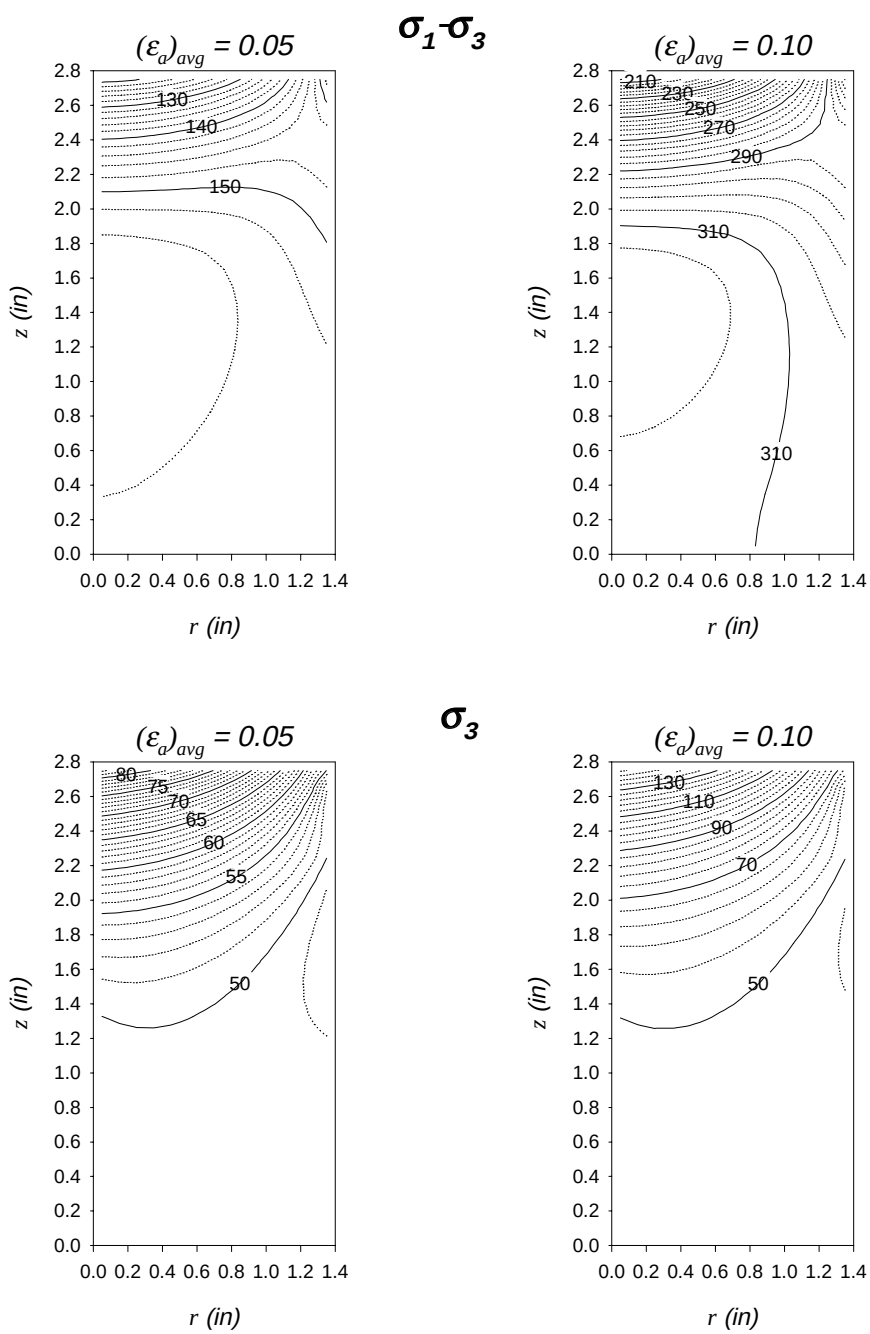

Figure 7.16 - Variation of Deviator and Confining Stresses for ϕ_{int} = 28.5°

Linear Elastic Model, ϕ_{int} = 28.5°
E = 3000 psi, ν = 0.495

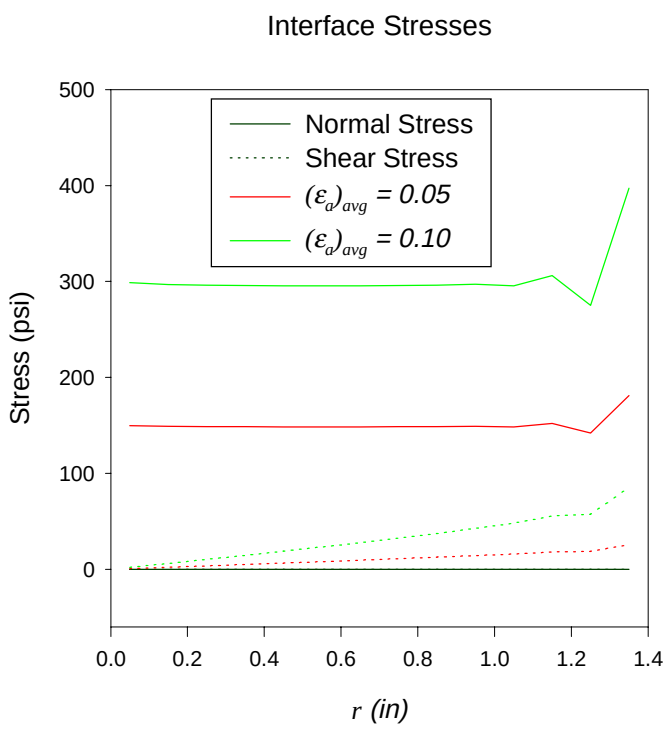

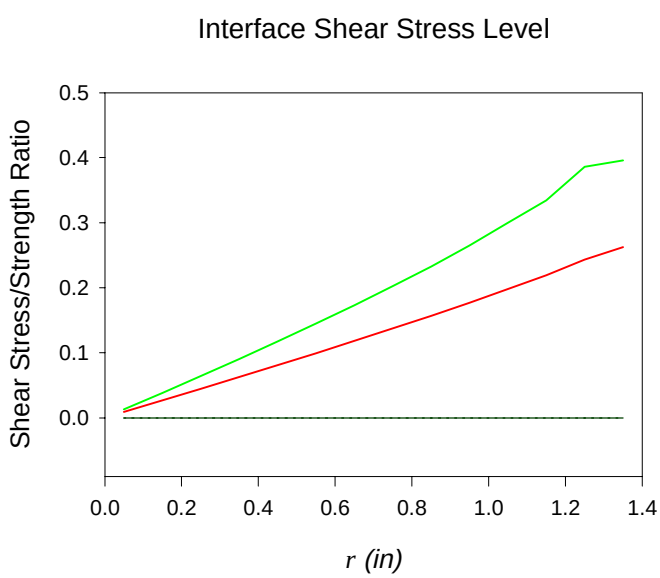

Figure 7.17 - Interface Stresses for ϕ_{int} = 28.5°

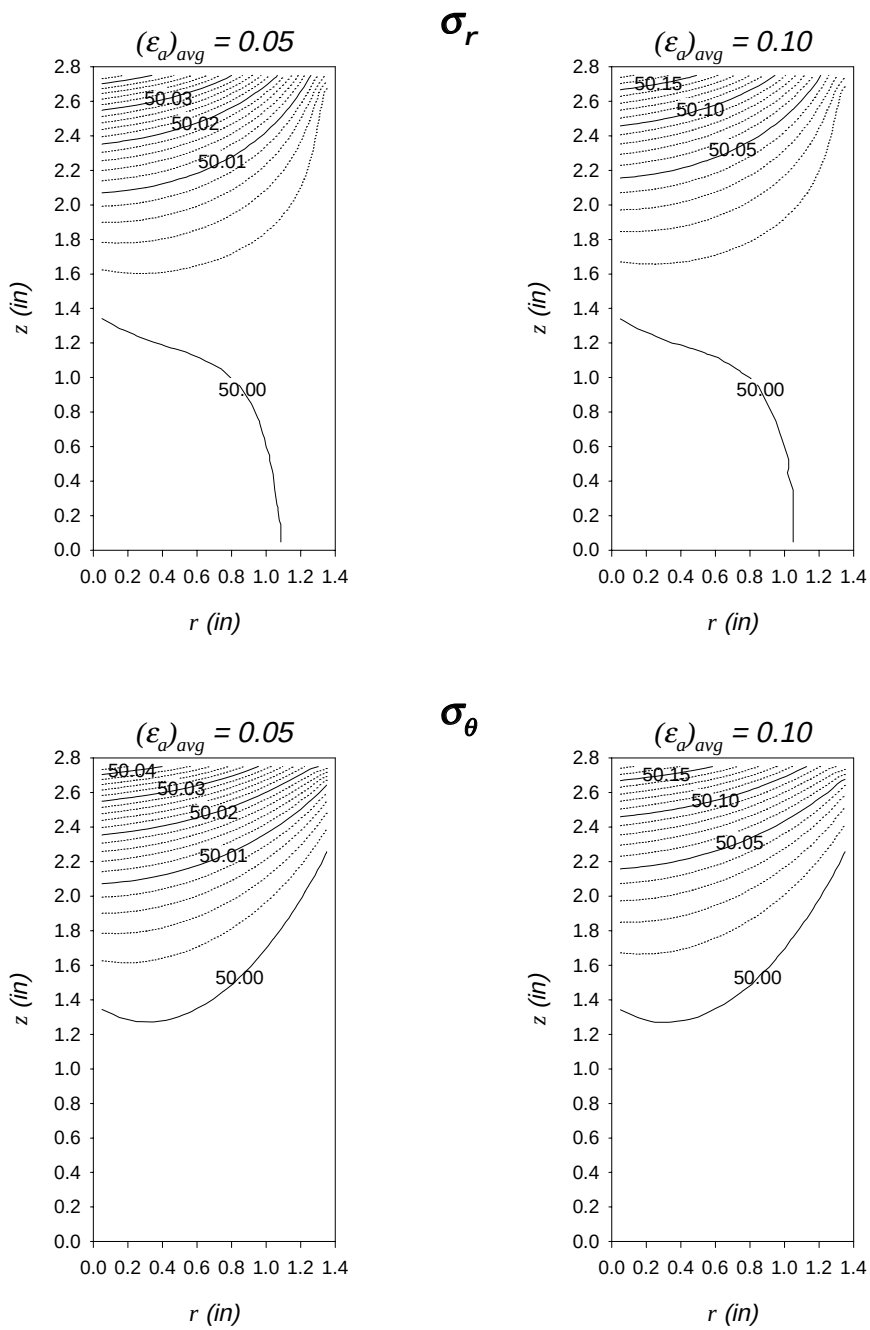

Figure 7.18 - Variation of Lateral Stresses for ϕ_{int} = 0.8°

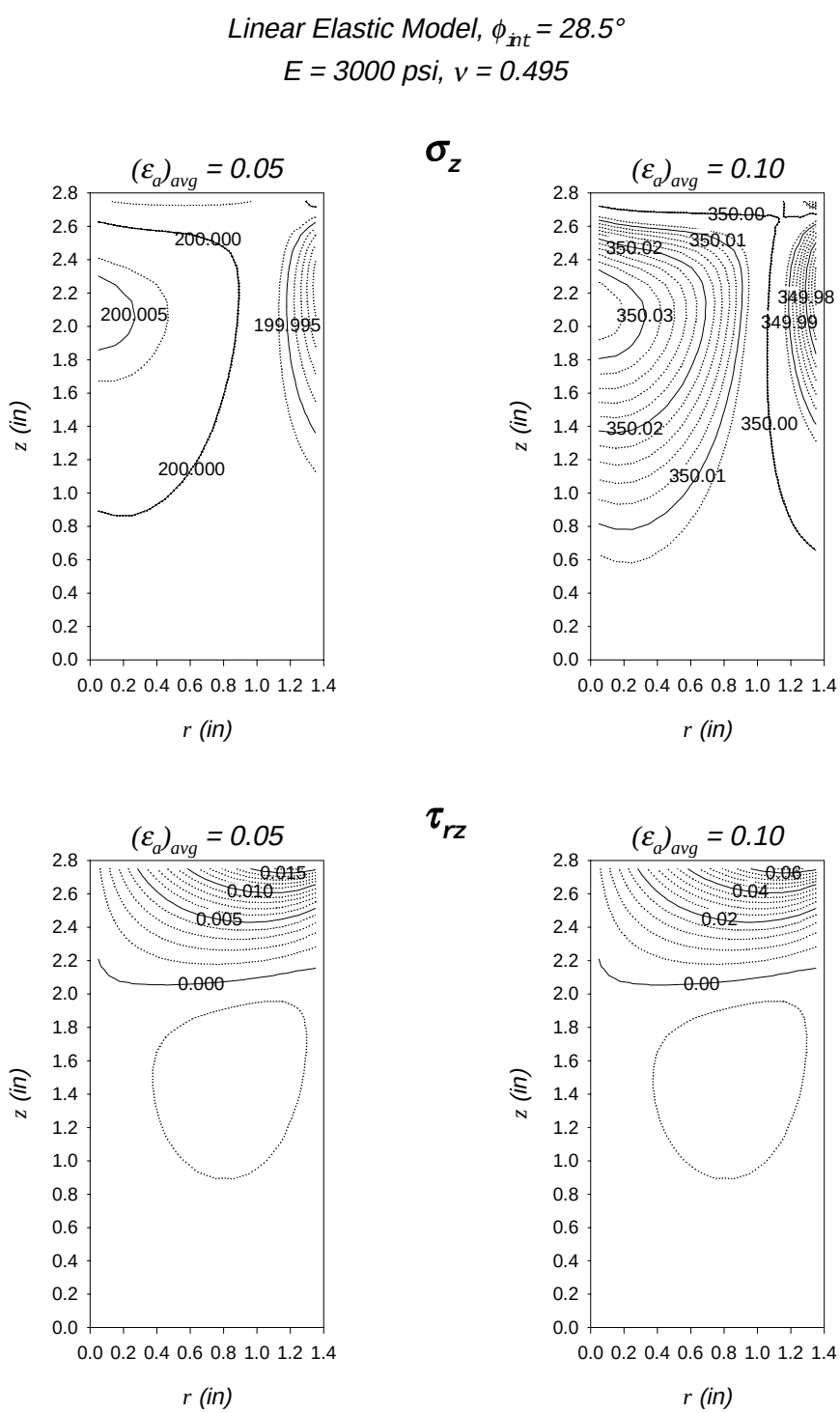

Figure 7.19 - Variation of Axial and Shear Stresses for ϕ_{int} = 0.8°

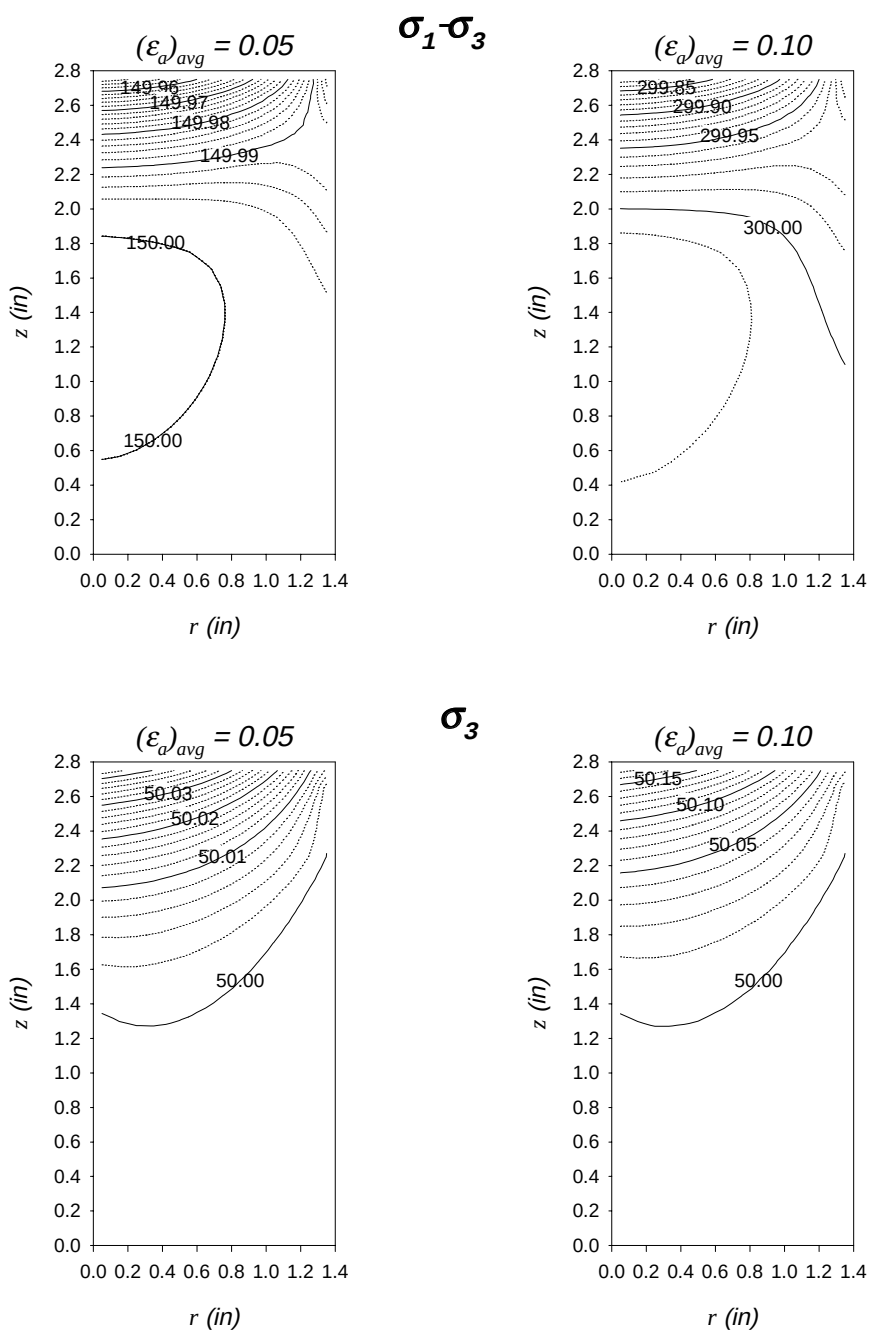

Figure 7.20 - Variation of Deviator and Confining Stresses for ϕ_{int} = 0.8°

Linear Elastic Model, ϕ_{int} = 28.5°
E = 3000 psi, ν = 0.495

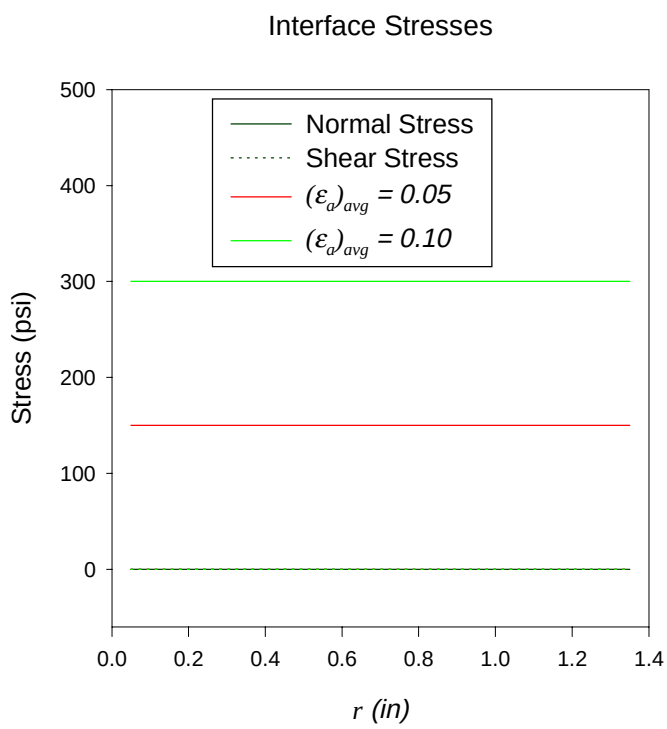

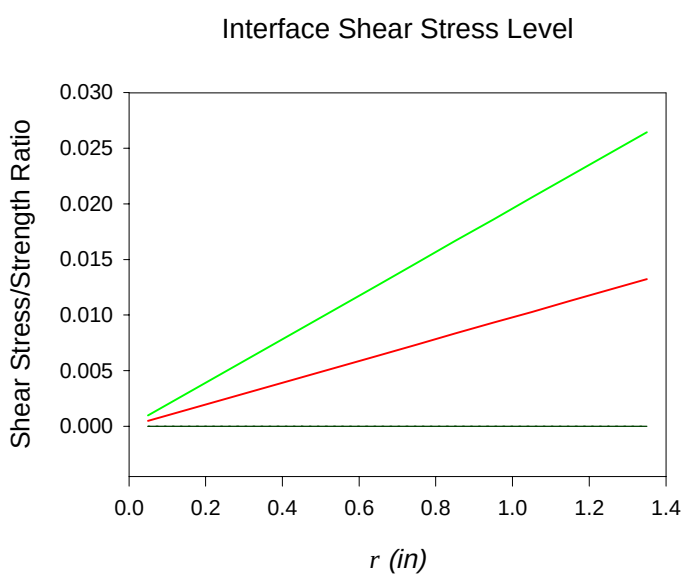

Figure 7.21 - Interface Stresses for ϕ_{int} = 0.8°

Summary of Effects on Linear Elastic Materials

For a ratio of specimen length to diameter of 1, the influence of end restraint conditions on measured stress-strain response and stress distributions within the specimen is significant. Increasing the value of L/D to 2 reduces the deviations in measured parameters and distributions of stresses within the specimen.

For a given L/D ratio and value of Poisson's ratio, the measured stress-strain response using restrained ends is still directly proportional to the value of elastic modulus. Thus, the variation in measured stress strain response can be normalized by the elastic modulus or by the *correct* stress (based on frictionless ends). The patterns of variation of the stresses within the specimen are independent of elastic modulus and the magnitude of these variations is directly proportional to the modulus value.

For a given L/D ratio, the significance of the effect of end restraint on measured stress-strain response increases as Poisson's ratio increases. Likewise, the magnitudes of the variations of stresses within the specimen are greater for higher values of Poisson's ratio. This phenomenon occurs because materials with higher values of Poisson's ratio exhibit greater tendency for lateral expansion during compression. Since end restraint inhibits this lateral expansion, its effect is more pronounced for materials with a greater tendency for lateral expansion.

Intermediate degrees of end friction result in similar patterns of variation of the stresses within the specimen, but the magnitude of these variations as well as the effect on the measured stress-strain response are less significant than for the case of complete end restraint. The effects of end restraint conditions on the measured stress-strain response for linearly elastic specimens at an axial strain level of 10 percent are summarized in Table 7.3.

Table 7.3 - Ratio of Measured to Correct Axial Stress at ε_a = 10%

Ratio of *Measured* Axial Stress to *Correct* Axial Stress				
	ϕ_{int} = 0.8° L/D = 2	ϕ_{int} = 28.5° L/D = 2	Pinned End L/D = 2	Pinned End L/D = 1
ν = 0.250	1.0000	1.0062	1.0181	1.0369
ν = 0.333	1.0000	1.0115	1.0344	1.0709
ν = 0.495	1.0000	1.0290	1.1189	1.2403

Drucker-Prager Elastic-Plastic Behavior (Incompressible)

Since the Drucker-Prager model includes linear elastic behavior prior to yield, the end restraint effects prior to yield should be similar to those exhibited by a linearly elastic material. Consequently, variations in the elastic properties will not be addressed using the Drucker-Prager model. Since the elastic properties of the specimen are the same as in the previous examples, the behavior of the specimen prior to any yielding should be identical. Because the stress state throughout the specimen is not uniform, some yielding can occur at lower strain levels than would be predicted based on average stresses.

For an elasto-plastic behavior of a uniform cylinder, compression between completely frictionless ends will result in uniform states of stress and strain throughout the specimen, since the material model itself does not induce any tendency for nonuniformity. The radial and circumferential stresses will be equal to the applied external pressure at all strain levels, and the axial stress initially will be equal to the applied external pressure, but will increase with strain level up to the yield point. After the onset of yielding, the states of stress will remain uniform with increasing strain. The states of stress and strain within the specimen can be summarized as follows:

$$\sigma_r = \sigma_\theta = \sigma_{cell} \qquad \varepsilon_r = \varepsilon_\theta = -\nu \cdot \varepsilon_a$$
$$\sigma_z = \sigma_{cell} + E \cdot \varepsilon_a \le \sigma_{cell} + \sigma_y \qquad \varepsilon_z = \varepsilon_a$$

where: σ_y = yield stress

The yield stress, based on the Mohr-Coulomb criterion, is a function of c and ϕ and the principal stresses. The elastic constants and shear strength parameters used for the analysis were:

$$E = 3000 \text{ psi} \qquad c = 0$$
$$\nu = 0.495 \qquad \phi = 36.87°$$

When the minor principal stress is equal to 50 psi, these parameters result in yielding at an axial strain level of 5 percent and a deviator stress of 150 psi for frictionless ends. Since the end effects may influence the occurrence of localized yielding within the specimen, the stress distributions were investigated at axial strain level below 5 percent, at 5 percent, and above 5 percent.

Figure 7.22 shows the measured stress-strain response, defined by external forces and displacements, and the correct stress-strain response, defined by the frictionless end condition, for elasto-plastic behavior. For the elastic portion of the stress-strain curve when yielding is not imminent, the apparent increase in stress due to the end effects is the same as for the linear elastic material. However, just prior to yielding, the measured stress is actually less than the correct stress. After significant plastic strains have occurred, the trend reverses again, so that the end effects appear to increase the stress. This phenomenon occurs because the shear stresses imposed on the specimen ends result in nonuniform distributions of stress within the specimen. Consequently, yielding does not occur in all elements at exactly the same time. Since some elements actually begin to yield prior to a strain level of 5 percent, the measured stress is slightly reduced. Likewise, at strain levels just beyond 5 percent, some elements have still not yielded, so the measured stress does not recover immediately. In general, the friction on the specimen ends has two influences on the measured stress-strain response: it increases the measured or average axial stress and softens the yield point in the stress-strain curve. Figure 7.23 shows the ratio of *measured* stress to *correct* stress, which further illustrates the phenomenon that occurs around the yield point as elements begin to yield at different strain levels. Figure 7.23 also demonstrates that for an interface friction angle of 0.8 degrees, the effects of end restraint on the measured stress-strain response is negligible, but that for an interface friction angle of 28.5 degrees, the effect can be significant, particularly at large strain levels. At

axial strain levels greater than approximately 12 percent, the apparent increase in stress is more than 10 percent.

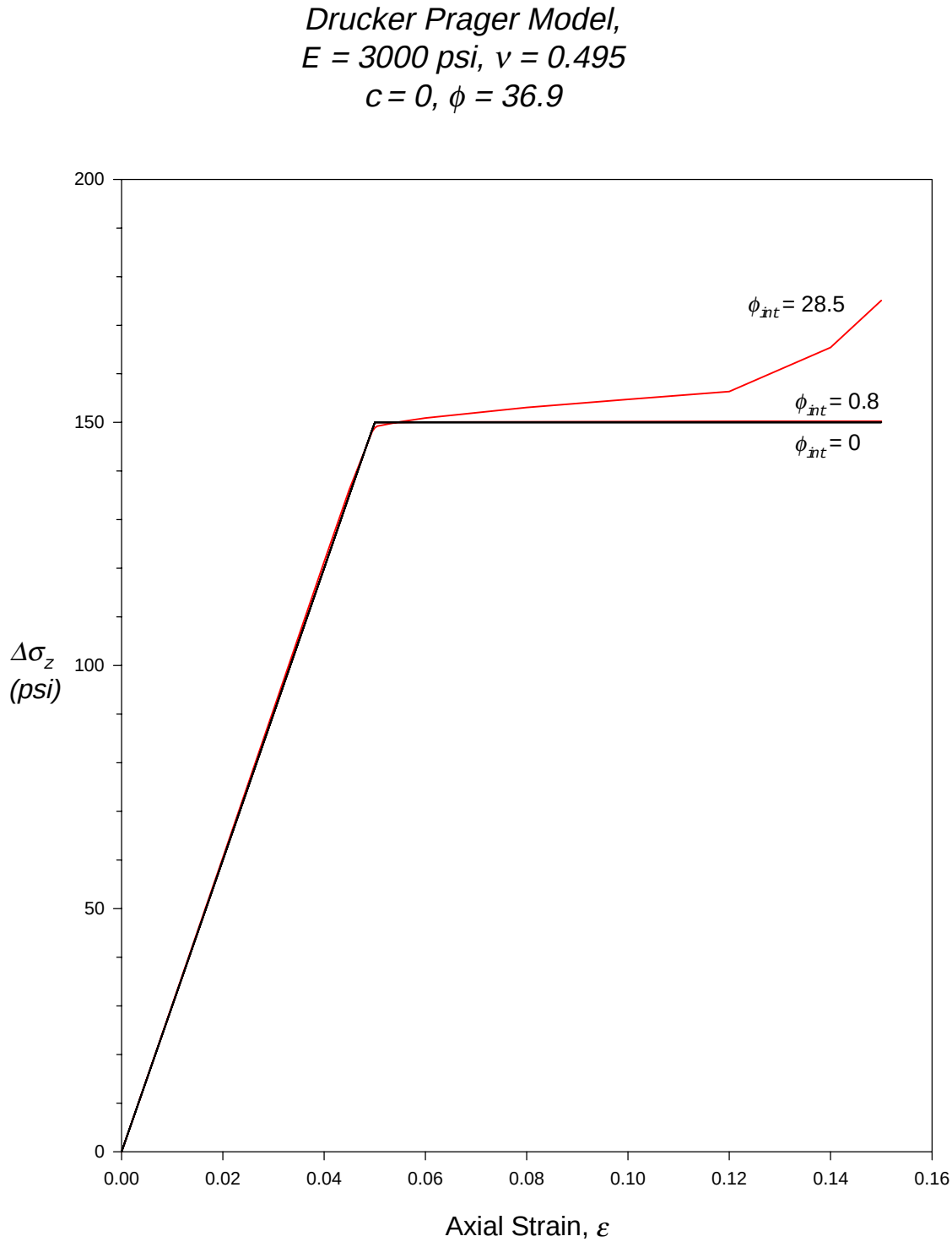

Figure 7.22 - Measured Stress-Strain Response for Elasto-Plastic Behavior

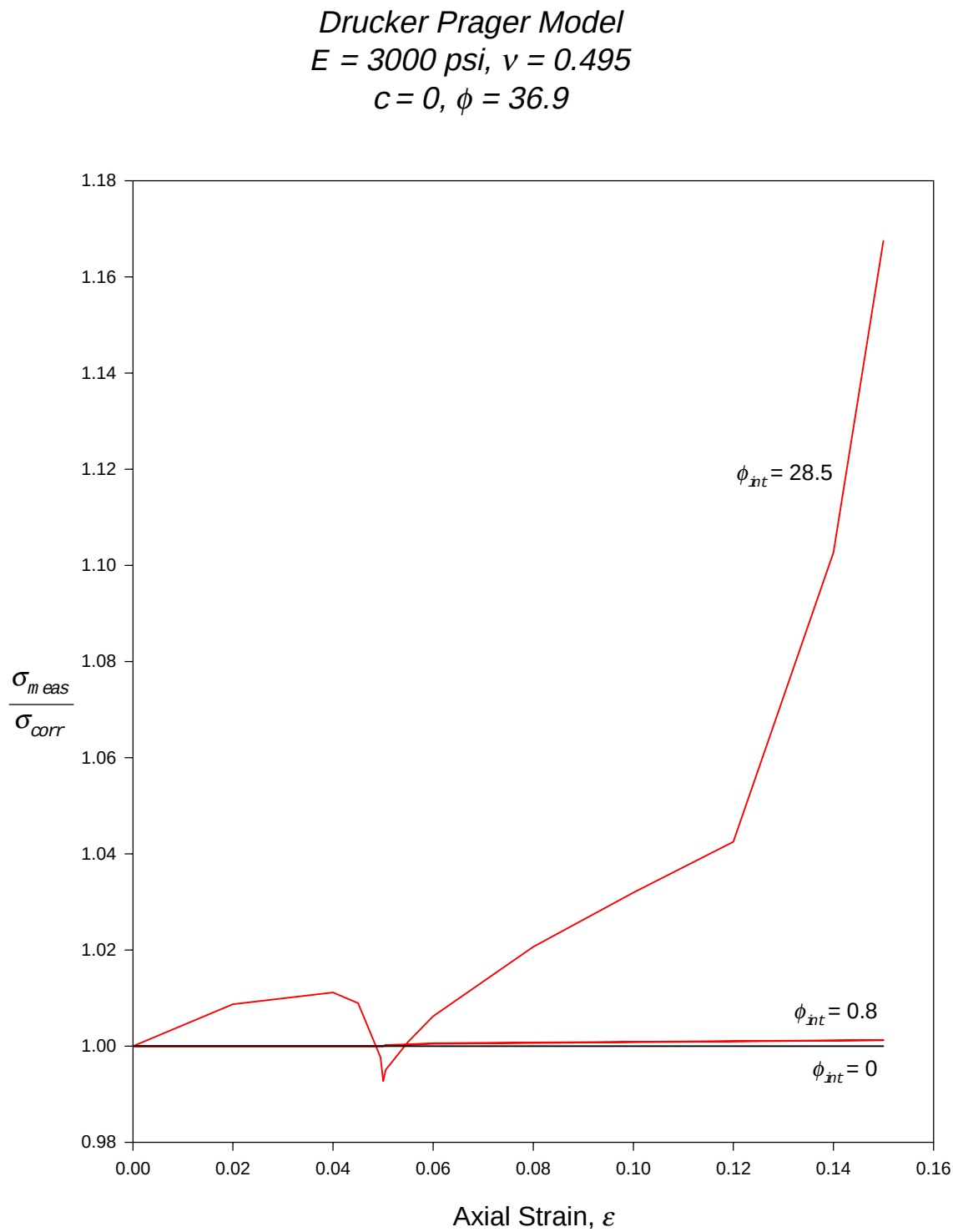

Figure 7.23 - Ratio of *Measured* Stress to *Correct* Stress for Elasto-Plastic Behavior

Conventional End Condition (ϕ_{int} = 28.5°)

Figure 7.24 shows the deviator and confining stress distributions at axial strain levels of 2 percent and 4 percent. These distributions are the same as those for the linear elastic cylinder at the same strain levels. The correct values of the deviator stress are 60 psi and 120 psi, respectively. The deviator stress decreases near the specimen ends and near the axis. The correct value of confining stress is 50 psi, and does not change with axial strain level. The confining stress increases significantly near the ends of the specimen, with the maximum occurring at the axis. Figure 7.25 shows the deviator and confining stresses at axial strain levels of 4.5 percent and 4.95 percent, at which the correct values of deviator stress are 135 psi and 148.5 psi, respectively. The patterns of variation are generally similar, although some change in the deviator stress distribution is noticeable. Figure 7.26 shows the deviator and confining stresses at axial strain levels of 5 percent, which is the yield point for compression between frictionless ends, and 5.05 percent. The correct deviator stress is 150 psi for both strain levels, since this value represents the strength of the specimen, and thus should not increase. Figure 7.26 demonstrates that only a small region of the specimen has actually yielded, since the deviator stress is less than 150 psi and the confining stress is at least 50 psi throughout most of the specimen. This region is located approximately halfway between the specimen mid height and the end near the axis. As the axial strain increases, the yielded region progresses toward the perimeter and the ends of the specimen as shown in Figure 7.27. Figure 7.28 shows the stress distributions at axial strain levels of 10 percent and 15 percent, and demonstrates that even at large strain levels, the elements near the ends of the specimen at the axis have not yielded. Since the yielding or failure is related to both the deviator stress and the confining stress, it is useful to normalize the distribution plots based on the failure surface, or yield criterion. For the Drucker-Prager model, the stress level can be defined as:

$$\frac{\sqrt{J_{2D}}}{\alpha \cdot J_1 + K}$$

When the stress level is equal to one, yielding occurs, and when the stress level is less than one, elastic deformation occurs. Figure 7.29, Figure 7.30, and Figure 7.31 show the distributions of stress level within the specimen at various strain levels. At an axial strain level of 4.95 percent, some local yielding is evident near the axis of the specimen, with the stress level decreasing near the ends. At an axial strain level of 5 percent, at which yielding would occur simultaneously in all elements using frictionless ends, the yielded region is expanding. With the exception of the regions near the ends, the specimen has yielded at an axial strain level of 5.5 percent. The extent of the non-yielding regions is within approximately 15 percent of the specimen length near each end. While more elements continue to yield as axial strain increases, Figure 7.31 shows that even at strain levels of 15 percent a significant portion of the specimen has yet to yield. Figure 7.32 shows the development of shear and normal stresses on the interface elements as axial strain increases. The plot of interface stress level indicates that none of the interface elements fail at axial strain levels up to 15 percent.

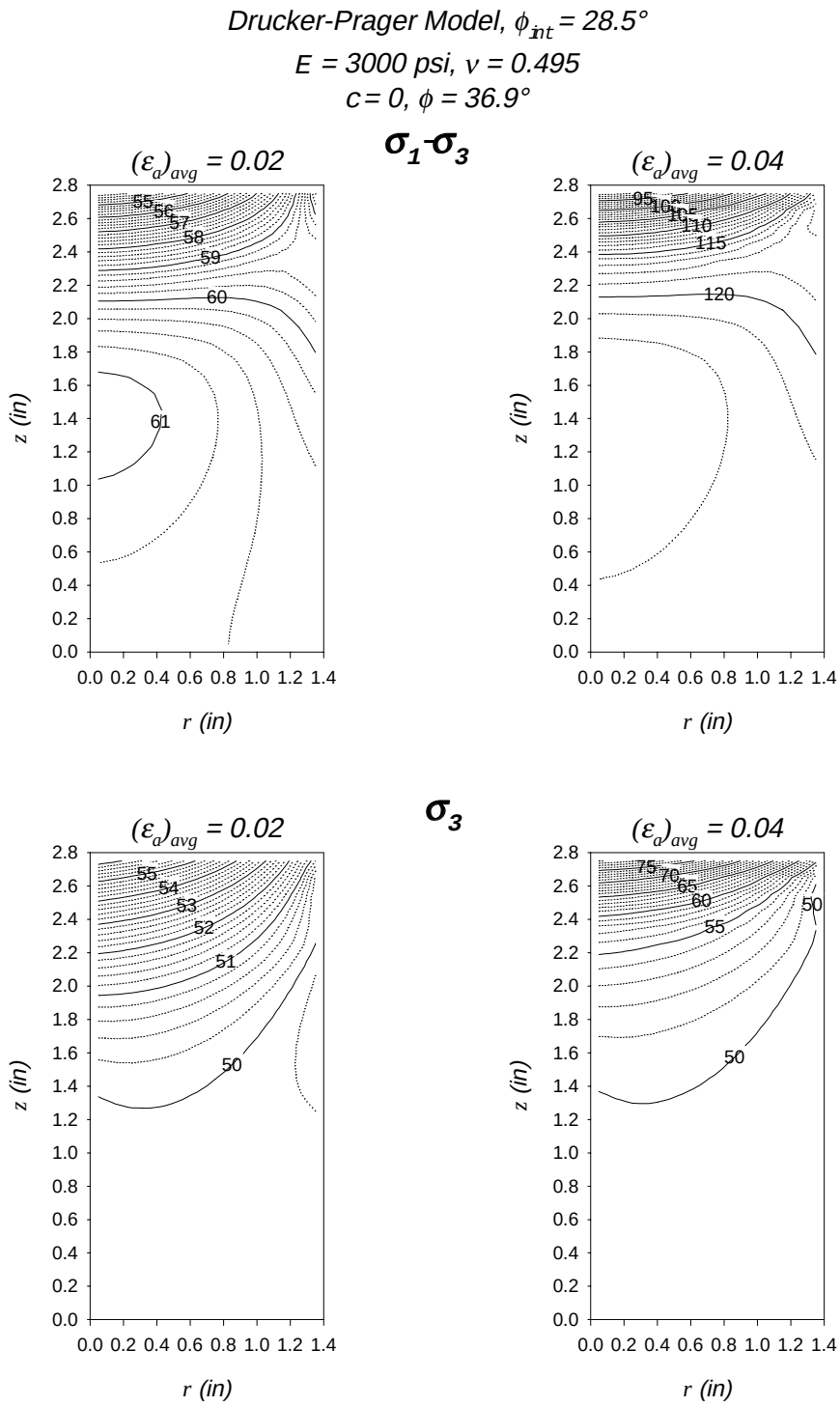

Figure 7.24 - Deviator and Confining Stresses in Elastic Range for ϕ_{int} = 28.5°

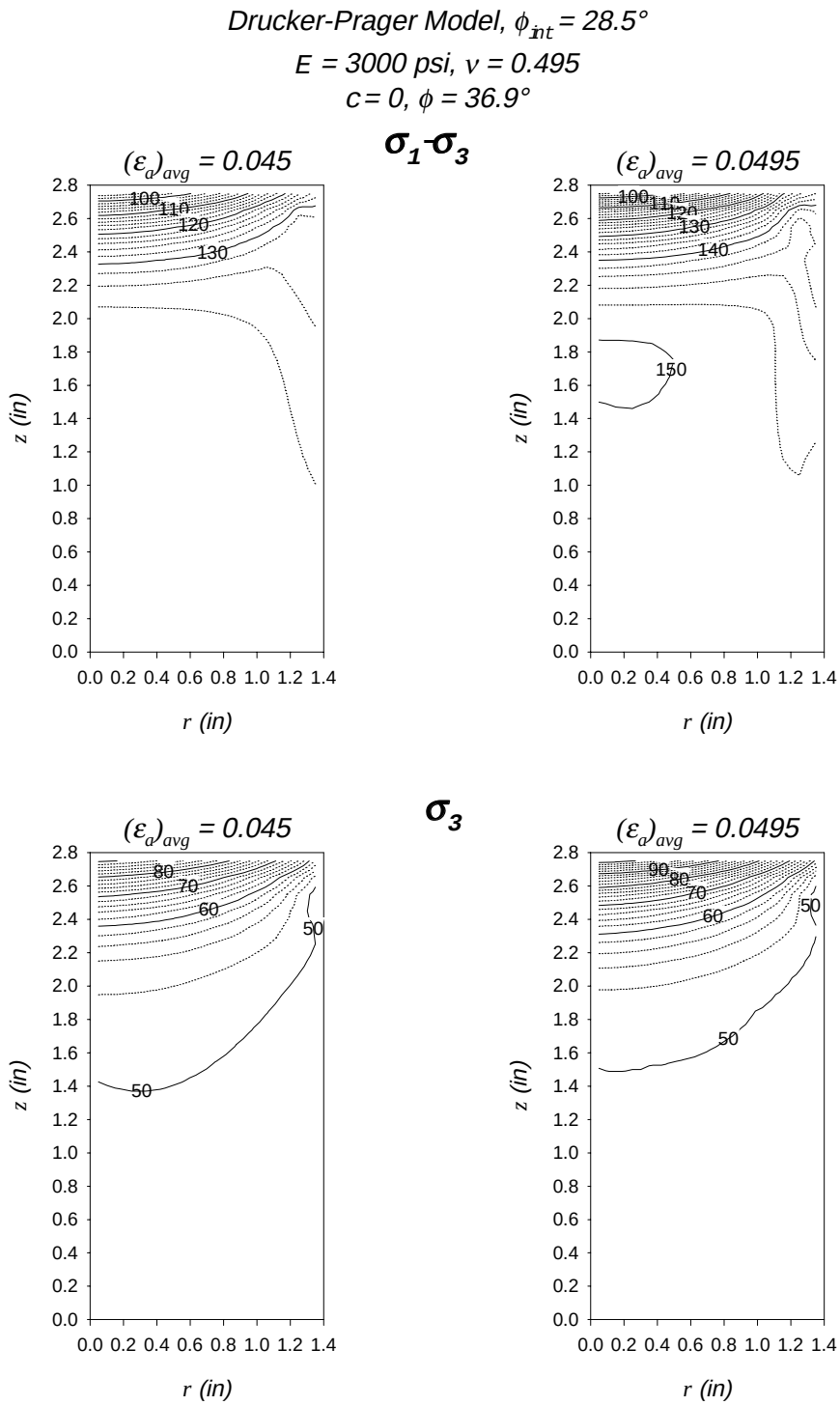

Figure 7.25 - Deviator and Confining Stresses Approaching Yielding for ϕ_{int} = 28.5°

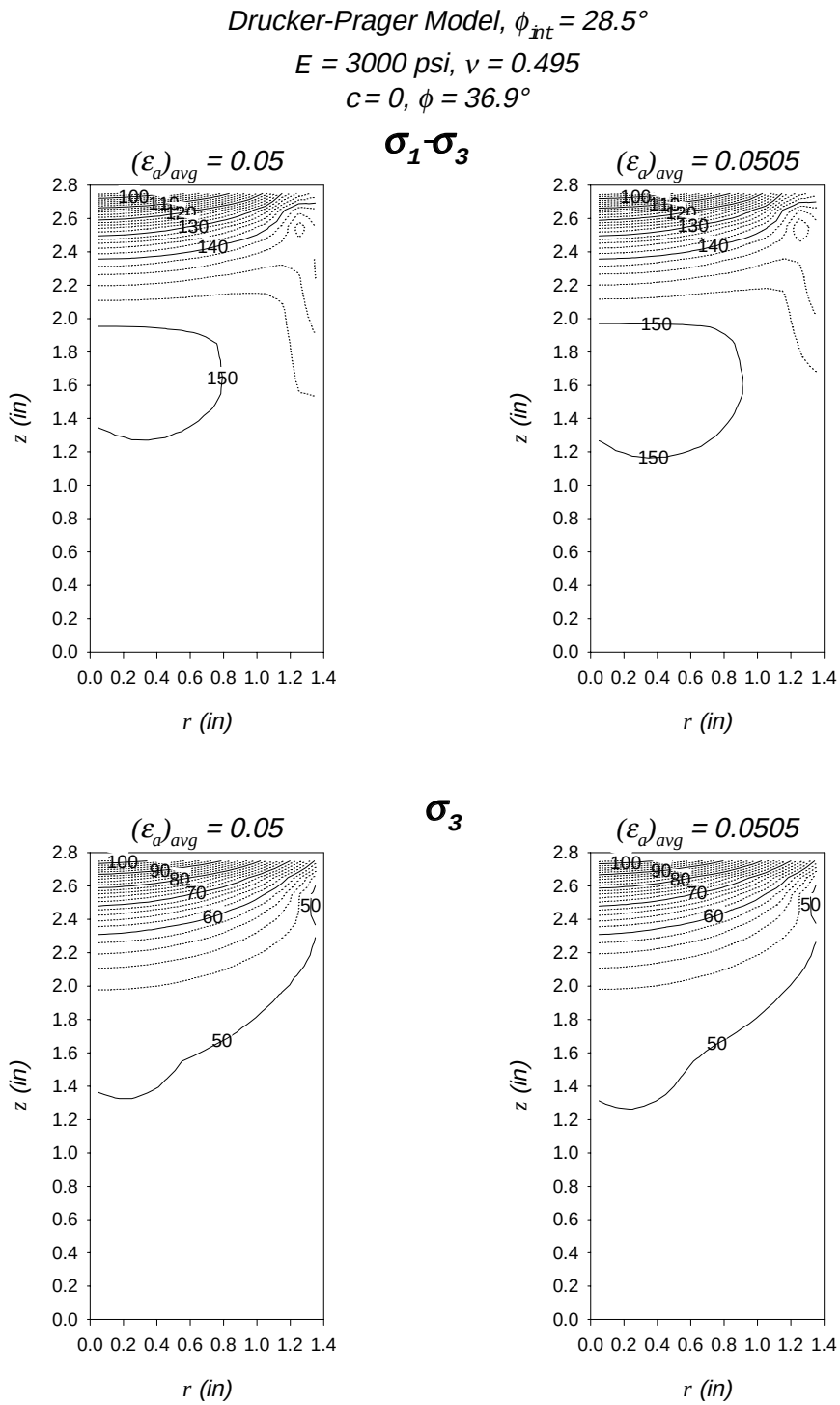

Figure 7.26 - Deviator and Confining Stresses During Yielding for ϕ_{int} = 28.5°

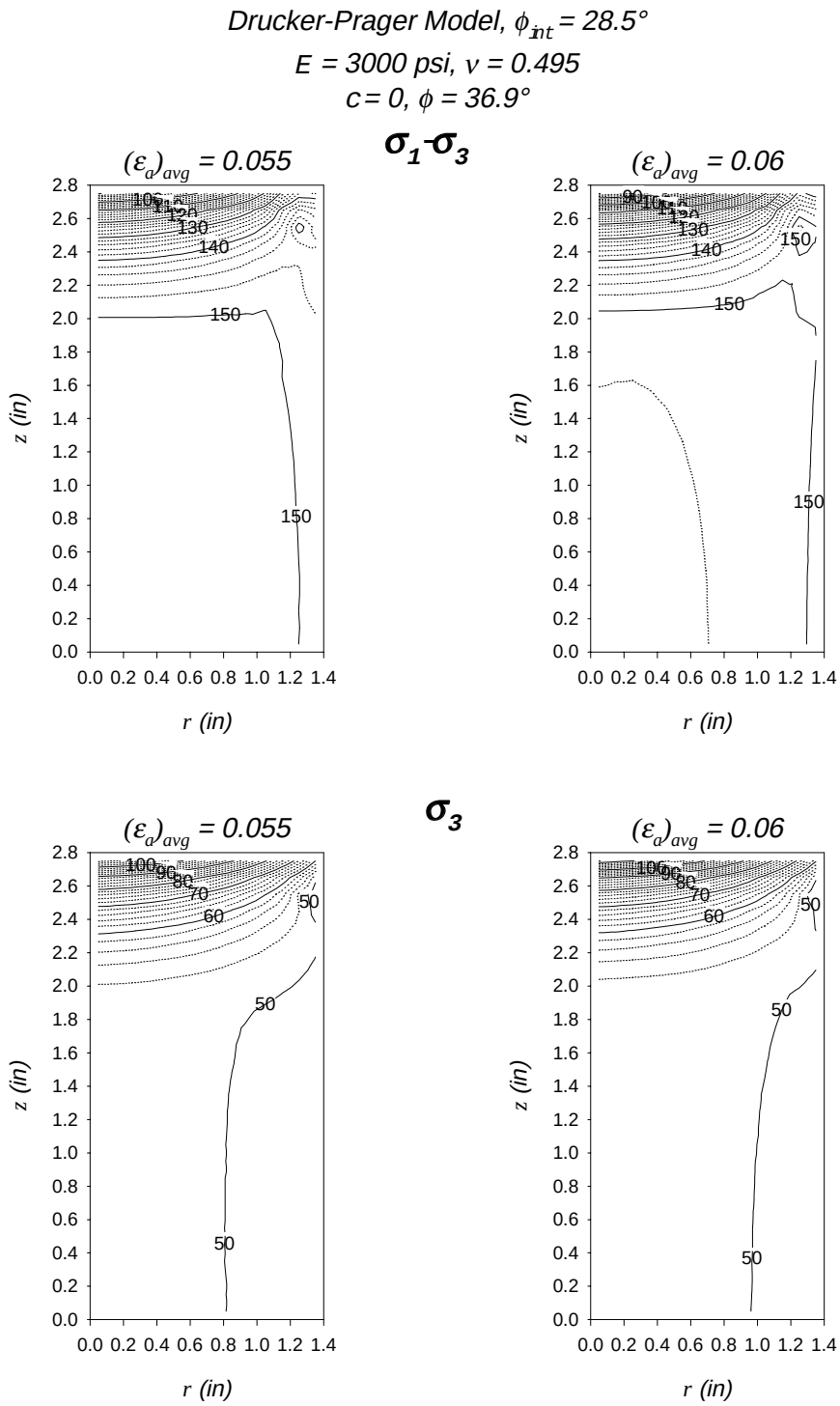

Figure 7.27 - Deviator and Confining Stresses Just After Yielding for ϕ_{int} = 28.5°

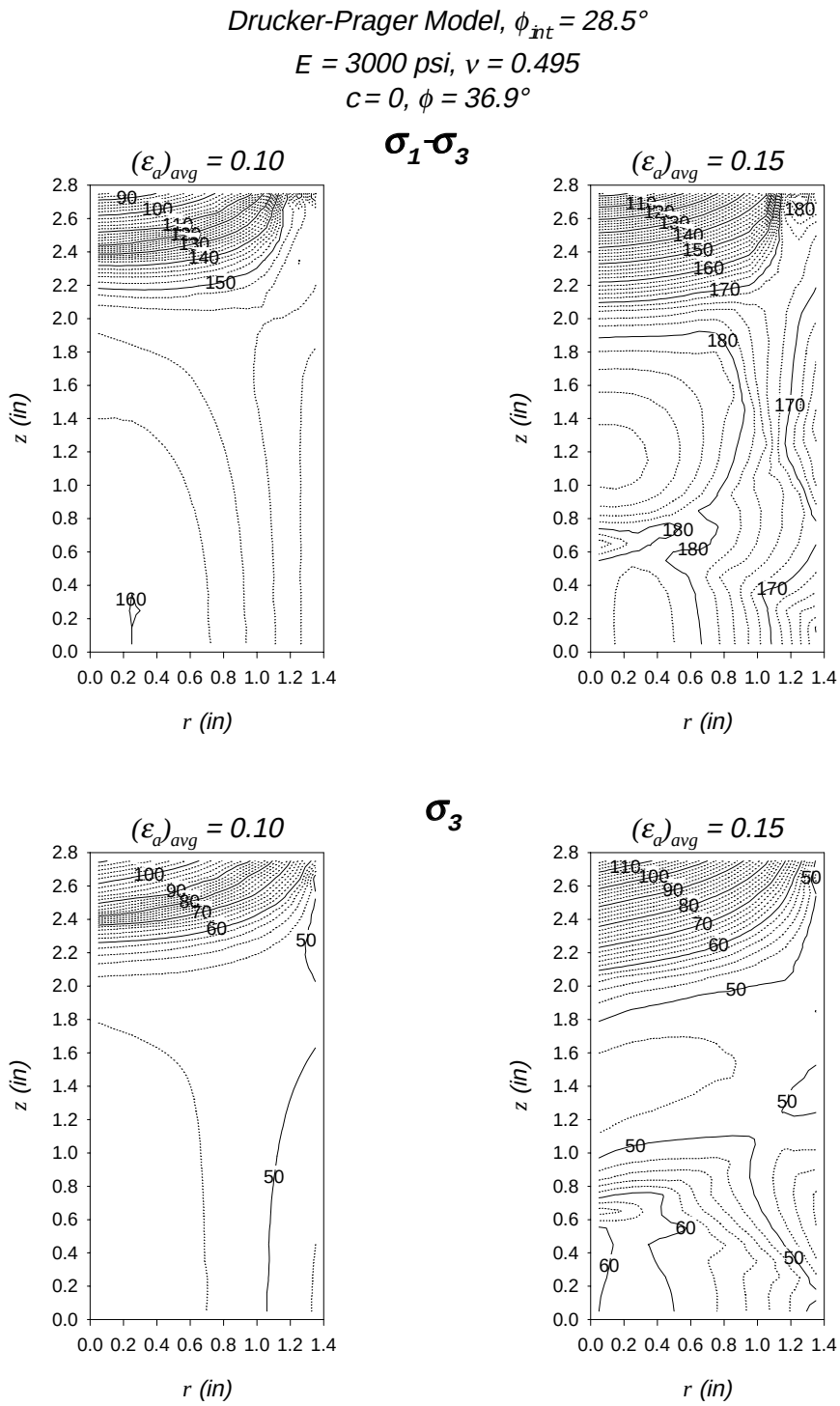

Figure 7.28 - Deviator and Confining Stresses at Large Strain for ϕ_{int} = 28.5°

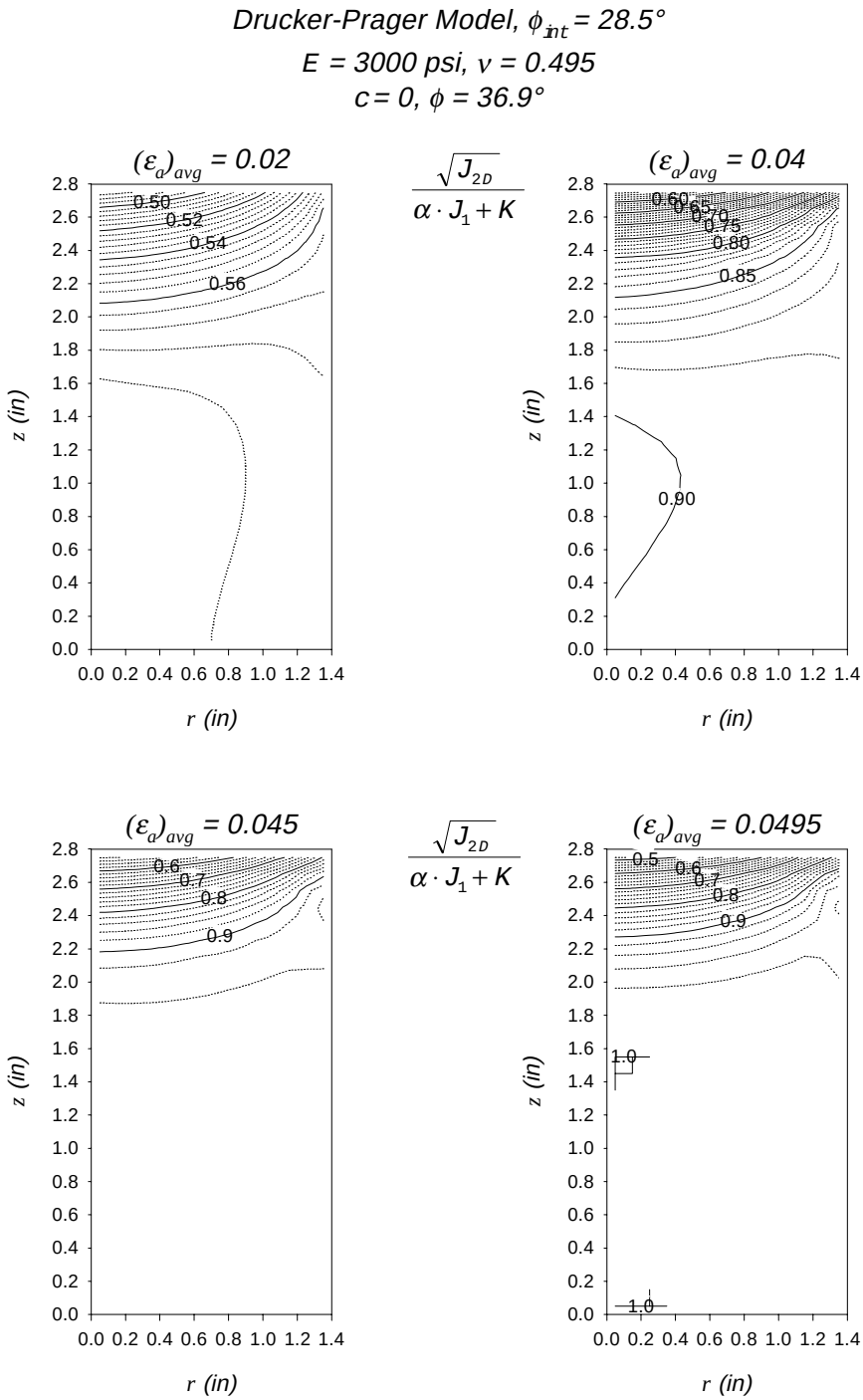

Figure 7.29 - Stress Level Prior to Yielding for ϕ_{int} = 28.5°

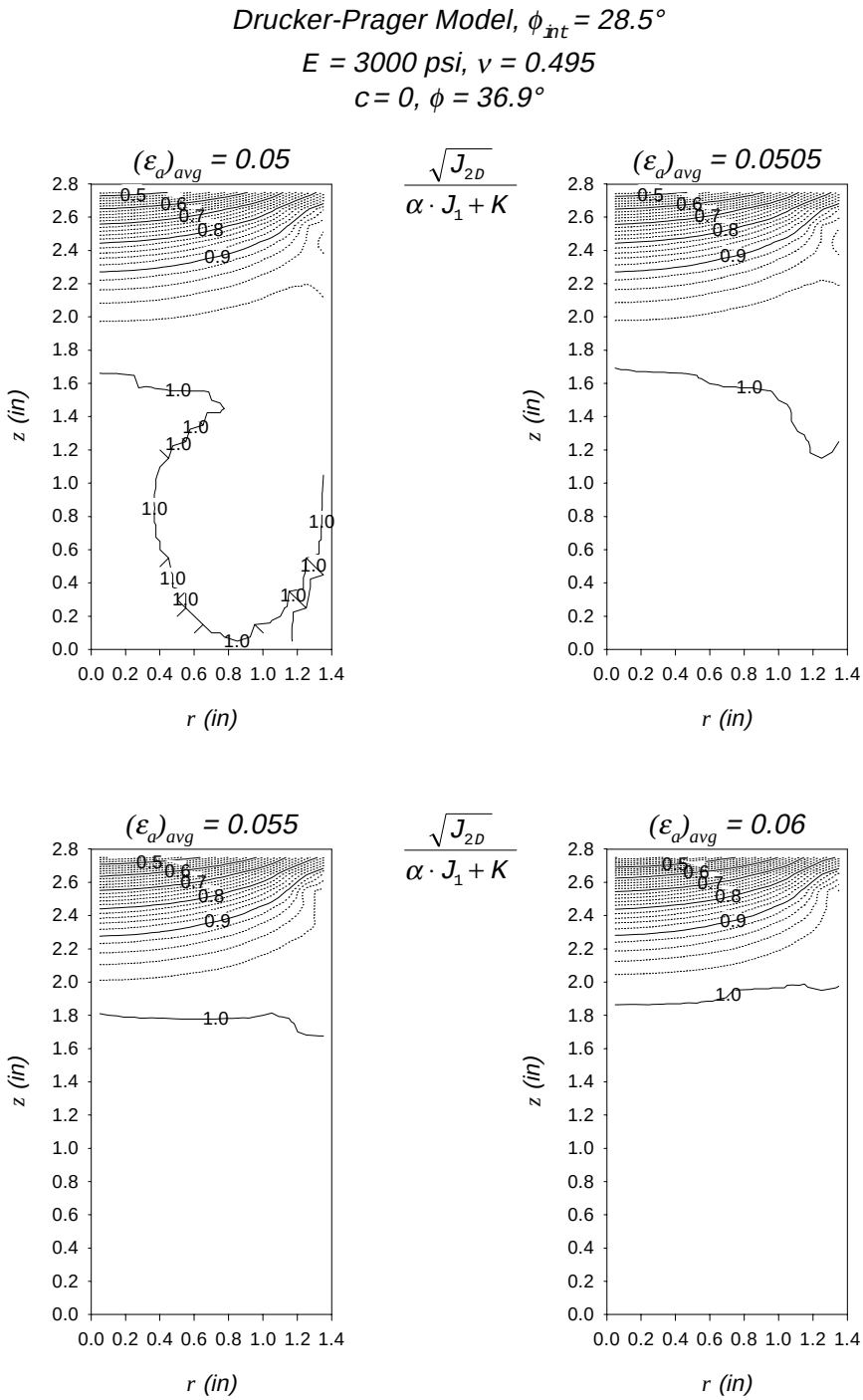

Figure 7.30 - Stress Level During Yielding for ϕ_{int} = 28.5°

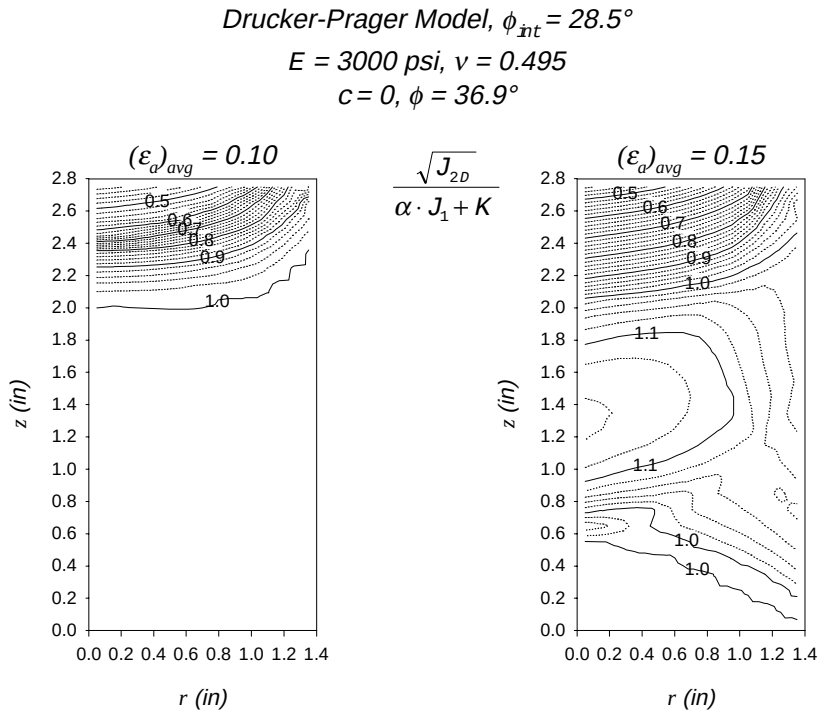

Figure 7.31 - Stress Level at Large Strain for ϕ_{int} = 28.5°

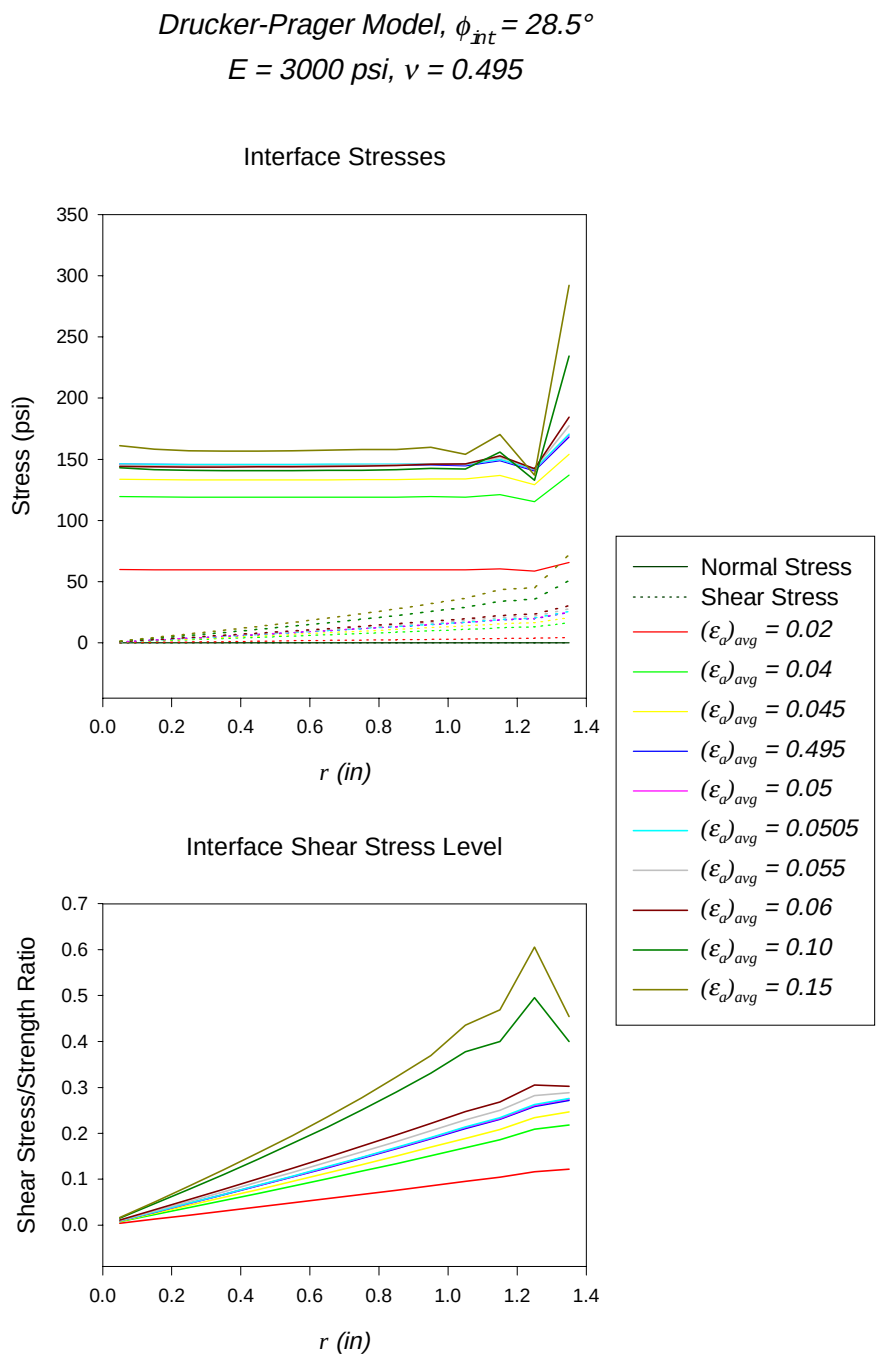

Figure 7.32 - Interface Stresses for ϕ_{int} = 28.5°

Lubricated End Condition (ϕ_{int} = 0.8°)

Figure 7.33, Figure 7.34, Figure 7.35, Figure 7.36, and Figure 7.37 show the deviator and confining stress distributions at various axial strain levels for an interface friction angle of 0.8 degrees. In general, the patterns of variation are similar to those corresponding to an interface friction angle of 28.5 degrees, but the magnitude of the variation is much less significant. For this case, the variations in the deviator stress and the confining stress appear to be negligible both prior to and after yielding. However, a significant change in the pattern of variation is observed at yielding that did not occur for the stronger, stiffer interface. Figure 7.37 shows a comparison of the patterns of variation in the elastic range and after significant plastic strains have occurred. The stress level distribution is plotted for various axial strain levels in Figure 7.38 and Figure 7.39. In contrast to the ϕ_{int} = 28.5° case, no progression of failure throughout the specimen is observed and all the elements appear to fail at nearly the same strain level. Unlike the ϕ_{int} = 28.5° case, all elements have failed at an axial strain level of only 5.05 percent, with no appreciable change in stress level throughout the specimen as strain increases. Figure 7.40 shows the development of shear and normal stresses on the interface elements as axial strain increases. The plot of interface stress level indicates that none of the interface elements fail at axial strain levels up to 15 percent.

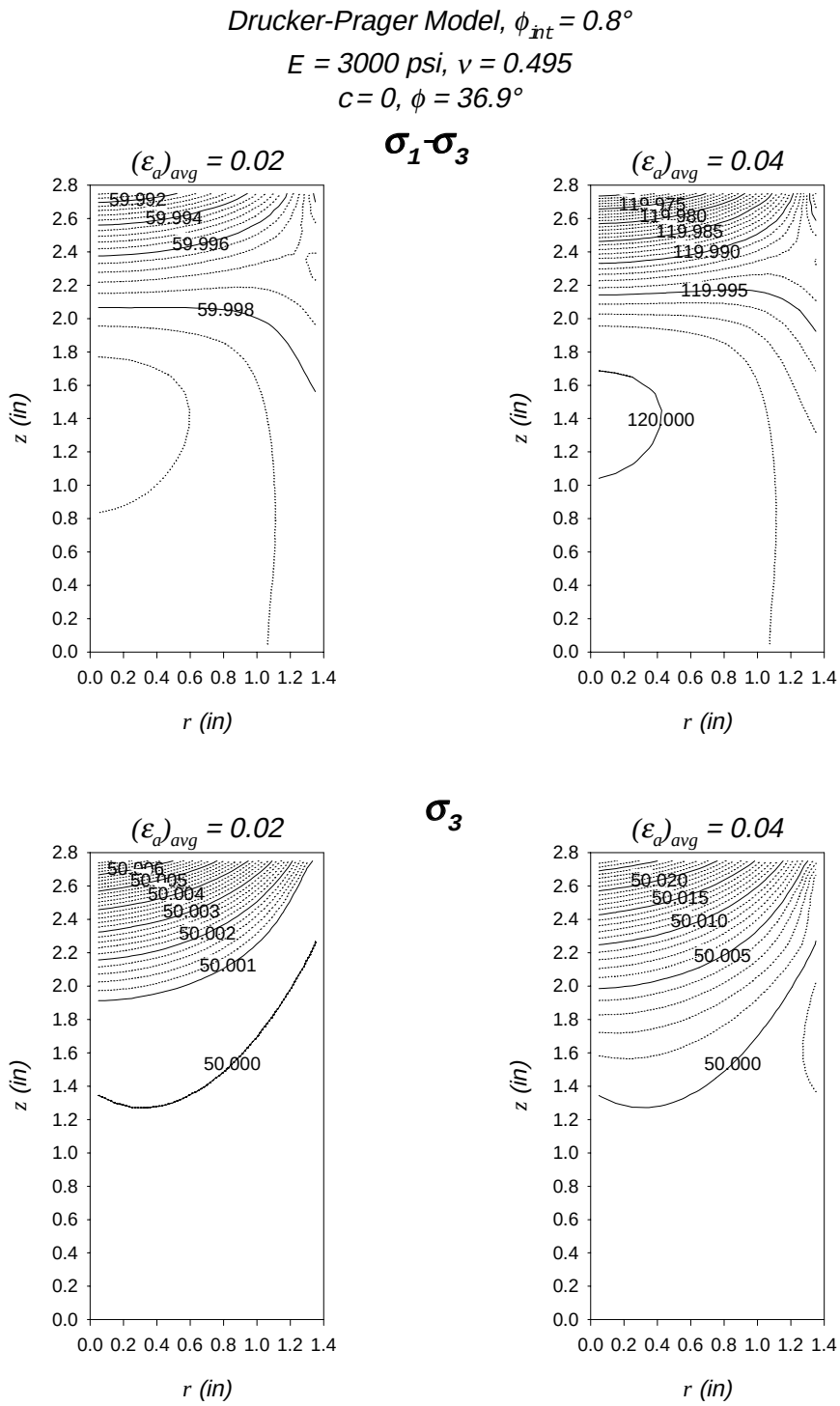

Figure 7.33 - Deviator and Confining Stresses in Elastic Range for ϕ_{int} = 0.8°

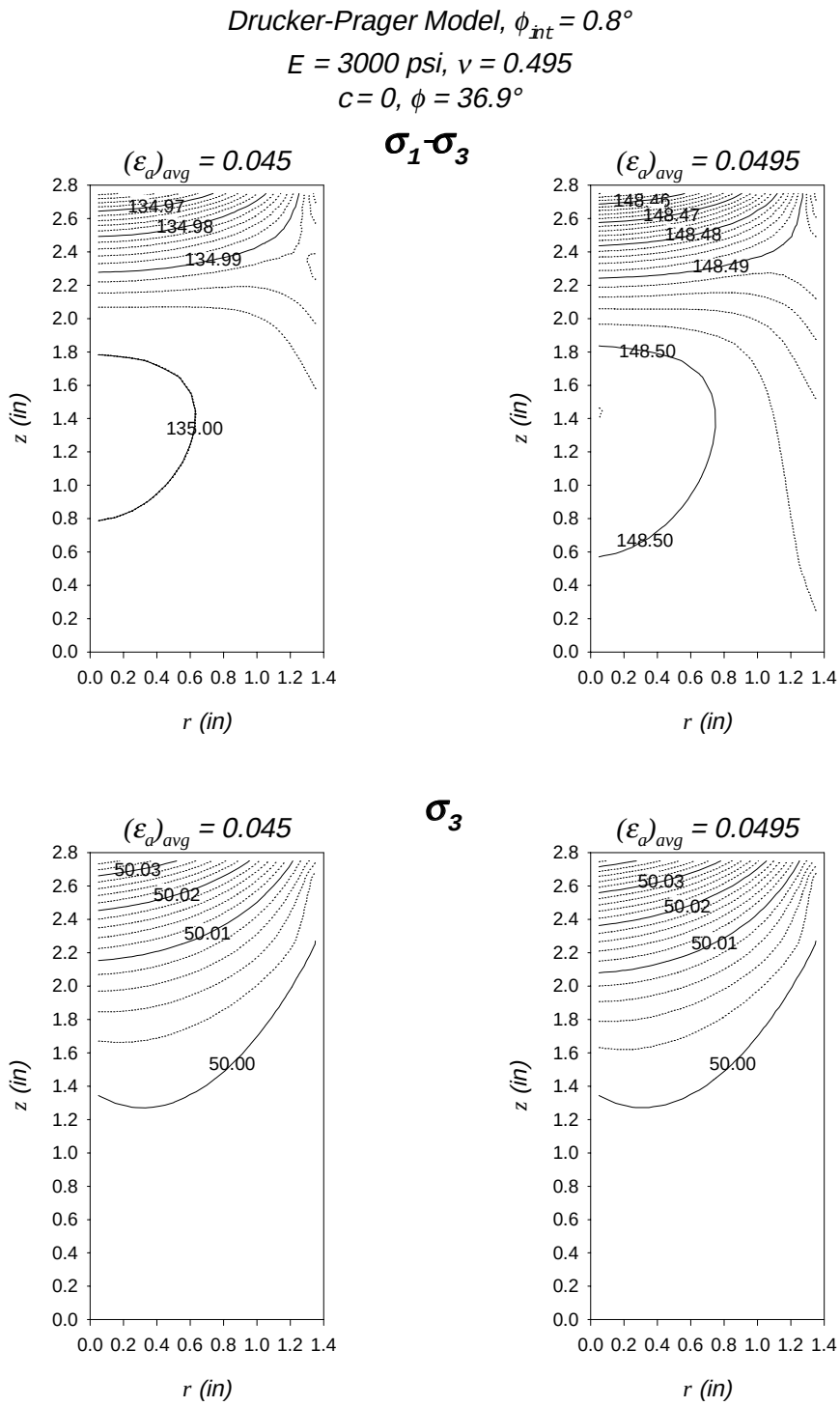

Figure 7.34 - Deviator and Confining Stresses Approaching Yielding for ϕ_{int} = 0.8°

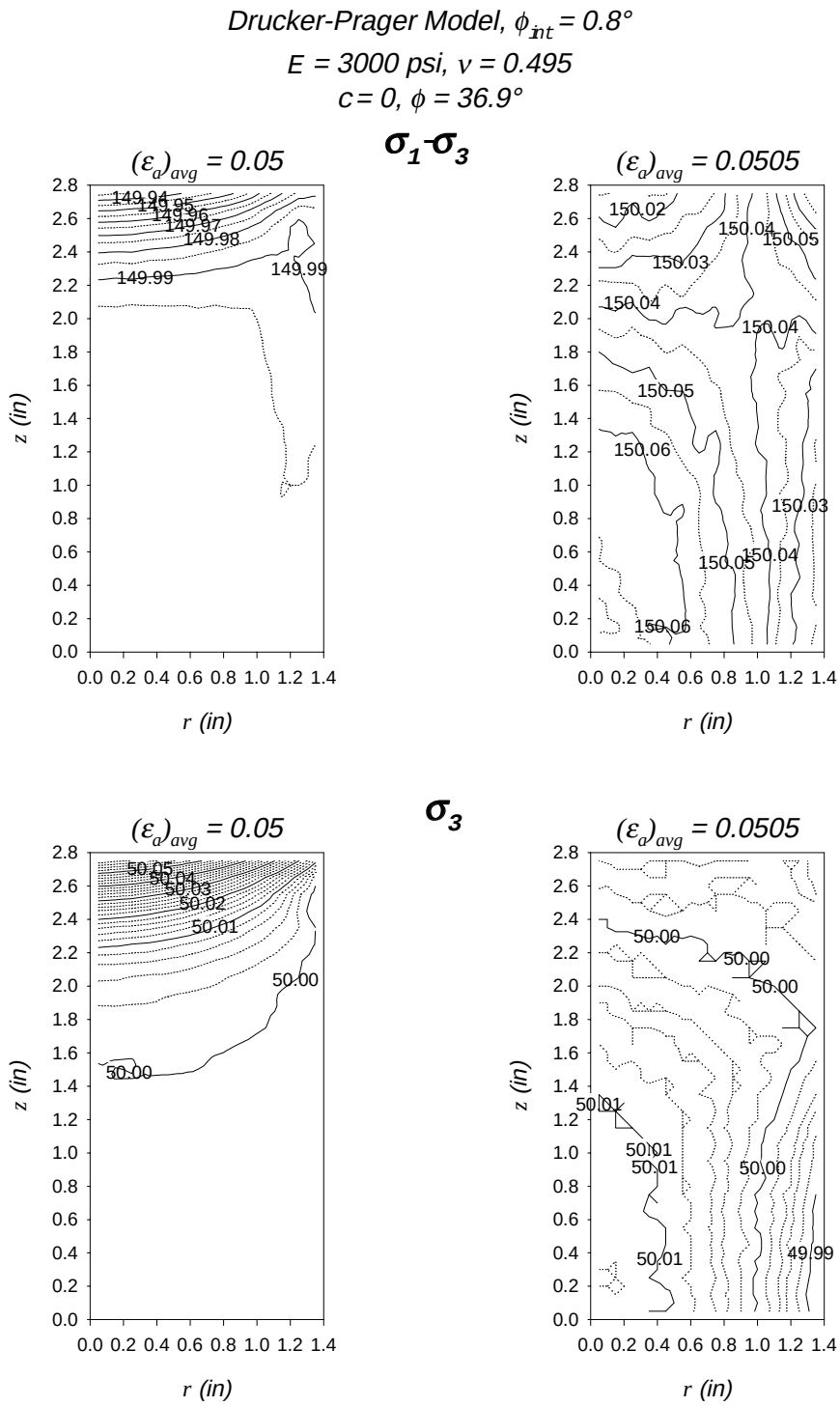

Figure 7.35 - Deviator and Confining Stresses During Yielding for ϕ_{int} = 0.8°

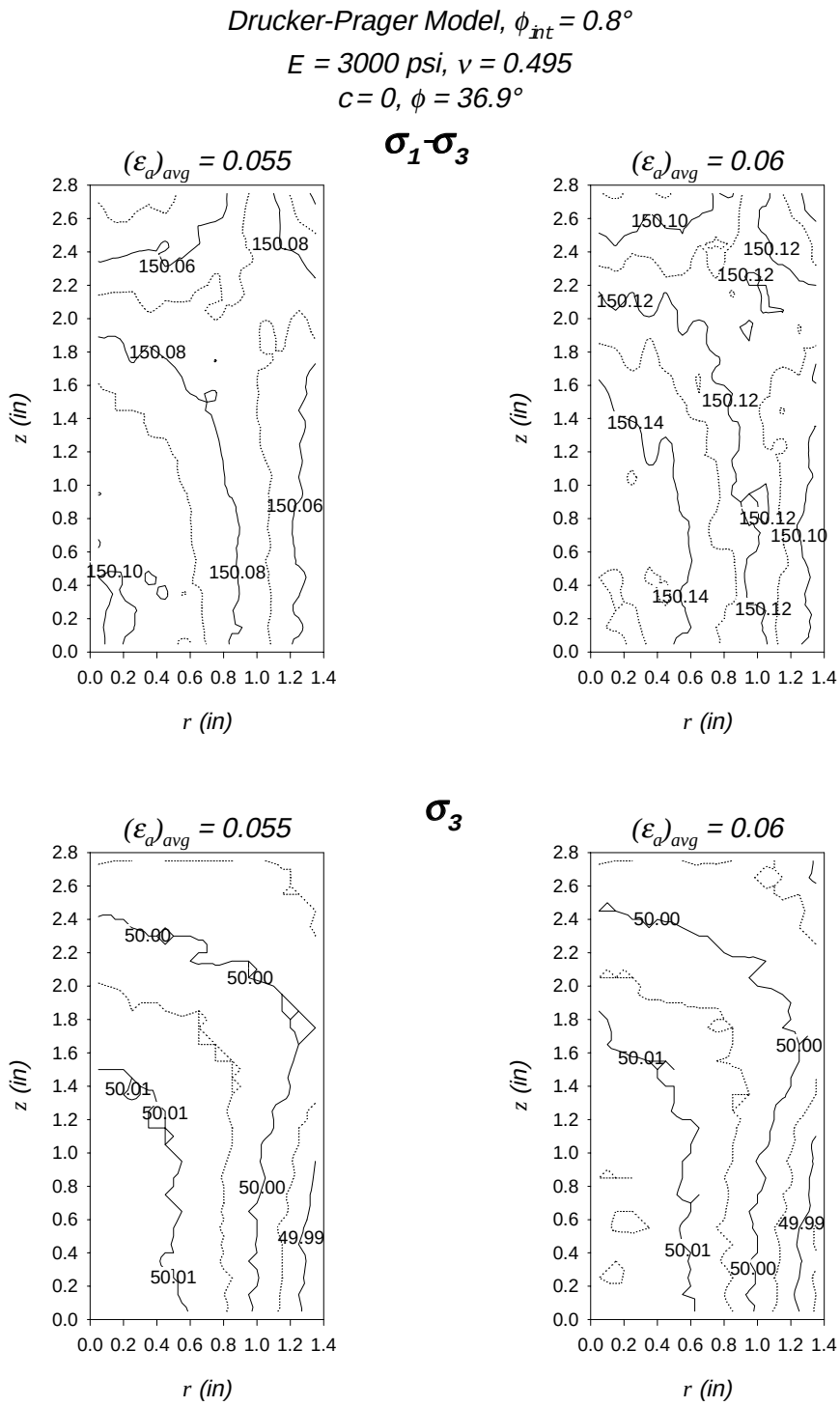

Figure 7.36 - Deviator and Confining Stresses Just After Yielding for ϕ_{int} = 0.8°

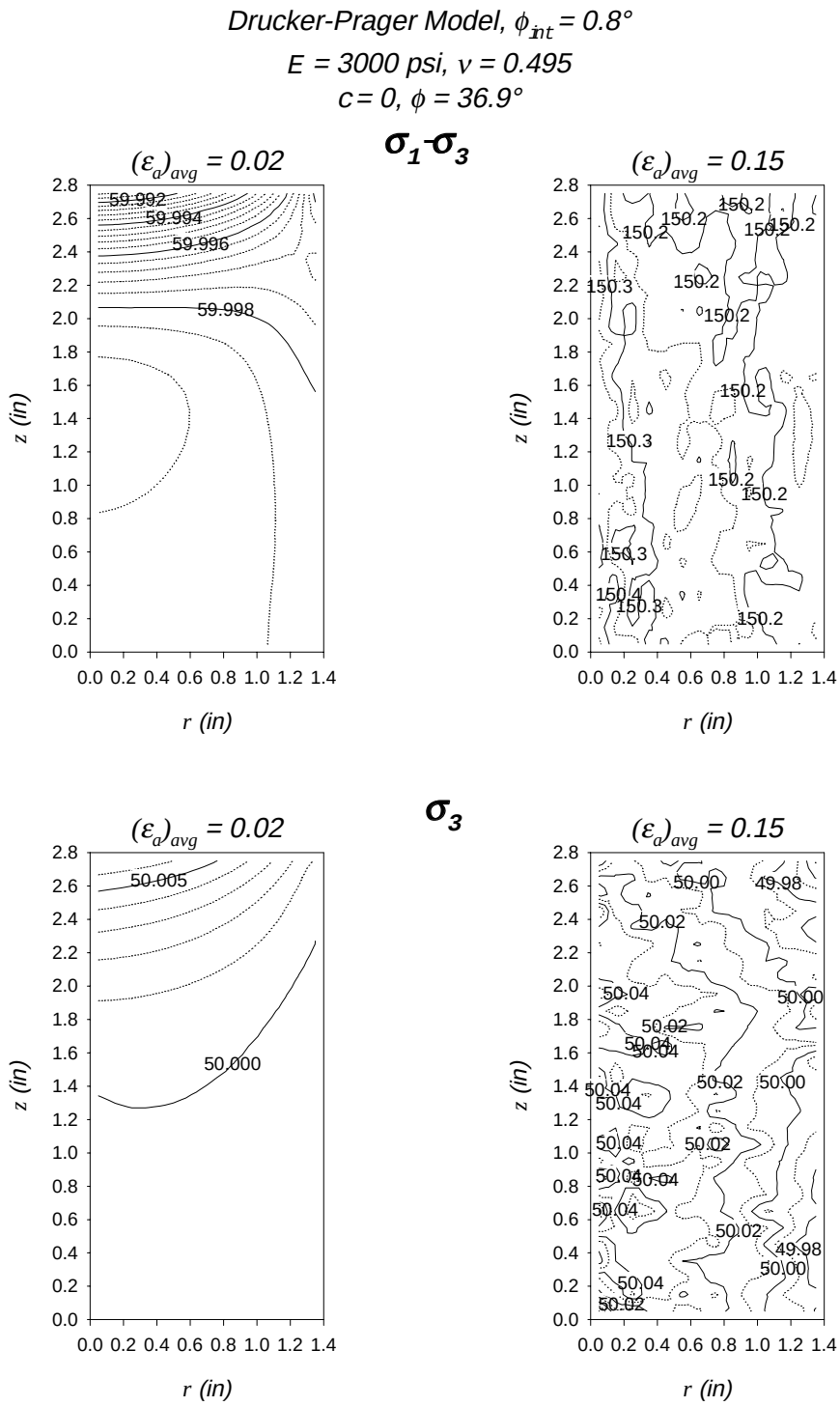

Figure 7.37 - Comparison of Stress Distributions in Elastic Range and Plastic Range for ϕ_{int} = 0.8°

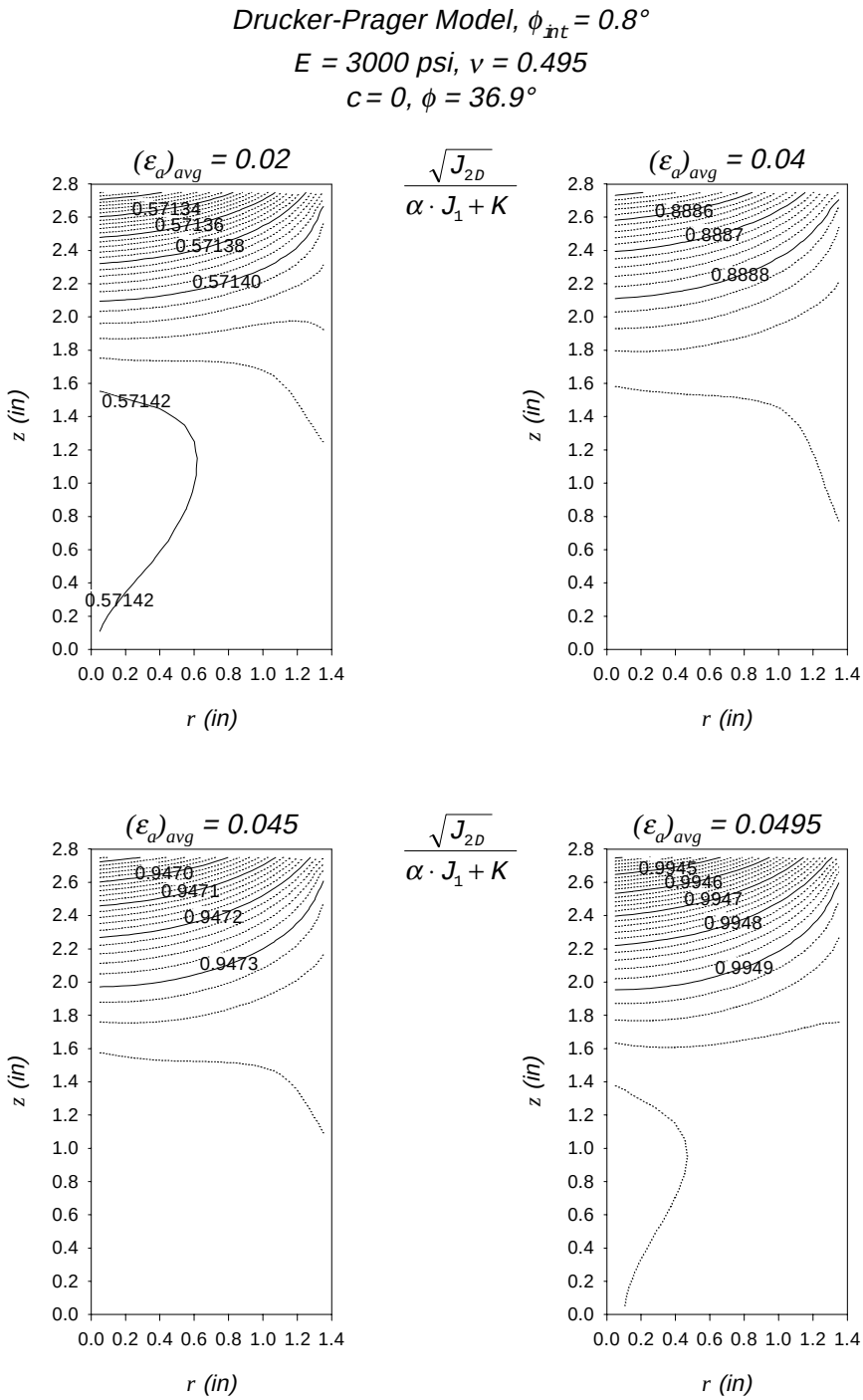

Figure 7.38 - Stress Level Prior to Yielding for ϕ_{int} = 0.8°

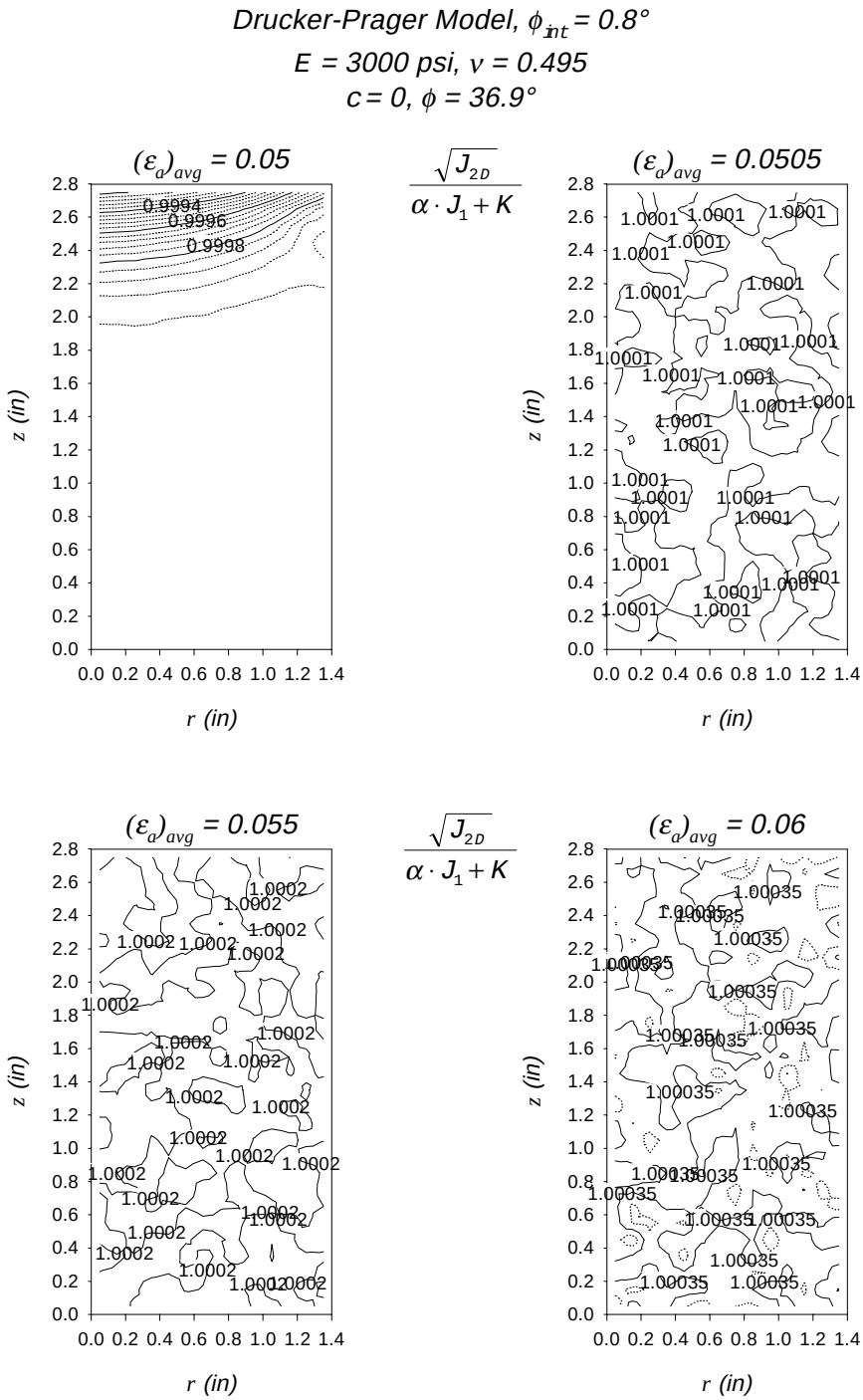

Figure 7.39 - Stress Level After Yielding for ϕ_{int} = 0.8°

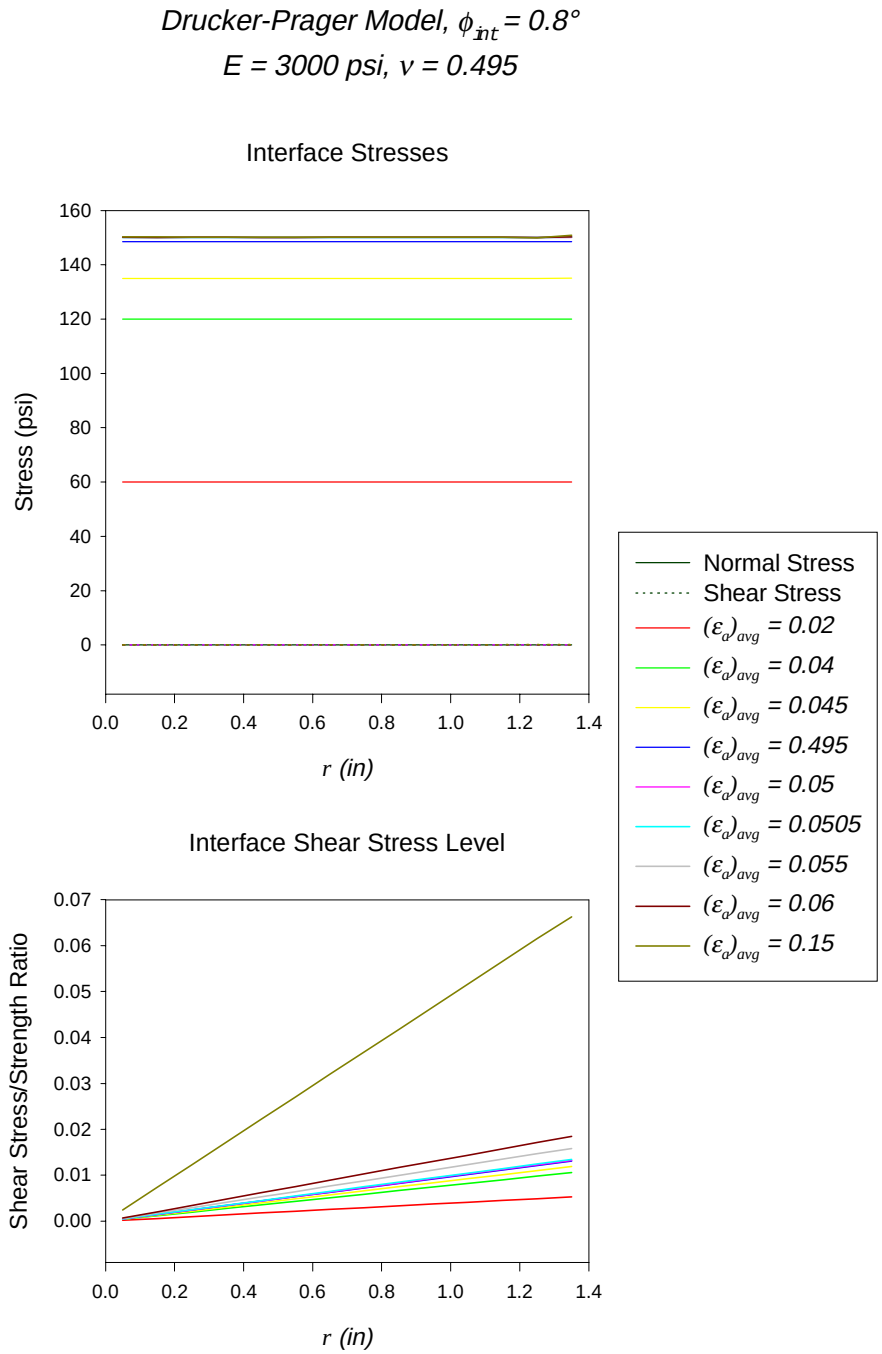

Figure 7.40 - Interface Stresses for ϕ_{int} = 0.8°

Summary of Effects on Elasto-Plastic Materials

Prior to yielding, the effects of end friction on the measured stress-strain response and the distributions of stresses within the specimen are the same for elasto-plastic and linearly elastic materials. The patterns of variation of the stresses within the specimen are independent of elastic modulus, but not Poisson's ratio.

The stress-strain curve is smoothed at the yield point due to the end friction effects. This occurs because the nonuniform stress conditions that develop within the specimen due to the induced shear stresses causes failure to occur progressively in the specimen, starting along the axis and halfway between the end and the mid-height of the specimen, and progressing toward the perimeter and the specimen ends. For the interface characteristics representing conventional end platens (ϕ_{int} = 28.5°) a portion of the specimen near the ends did not fail at axial strain levels up to 15 percent, when failure would have occurred at 5 percent axial strain if the ends were frictionless. For the interface characteristics representing lubricated end platens (platens (ϕ_{int} = 28.5°) all soil elements failed, and failure occurred at nearly identical strain levels for all elements. In neither case did any of the interface elements fail at axial strain levels up to 15 percent.

The effects of end friction conditions on the measured stress-strain response for elasto-plastic specimens at various axial strain levels are summarized in Table 7.4.

Table 7.4 - Ratio of *Measured* Axial Stress to *Correct* Axial Stress

Ratio of *Measured* Axial Stress to *Correct* Axial Stress		
Axial Strain Level	ϕ_{int} = 0.8°	ϕ_{int} = 28.5°
ε_a = 0.02	1.000	1.009
ε_a = 0.05	1.000	0.993
ε_a = 0.10	1.001	1.033
ε_a = 0.15	1.001	1.167

Summary

The finite element analyses performed were valuable for investigating the influence of various degrees of end restraint on the measured stress-strain characteristics of the specimen. They also demonstrated the extent of the nonuniform distributions of stresses that develop in the specimen during compression as a result of the shear stresses that are induced by the friction on the specimen ends. Although the analyses performed have limited application to predicting the actual material response of a triaxial specimen during an undrained test, it must be remembered that the purpose of the analyses was to investigate the influence of varying degrees of specimen end friction on the stress conditions in the specimens, not to accurately predict material behavior observed during actual tests. Overcoming some of the limitations of the analyses performed might further the understanding of end platen conditions as well as other influences on actual test conditions that result in deviations

from assumed conditions. The material models employed in these analyses satisfactorily modeled the zero volume change condition, but did so on an element-by-element basis. An effective stress-based constitutive model that could predict the coupled volume change and pore pressure development during compression and shear would better represent actual tests conditions because the zero volume change condition could be enforced at the specimen boundaries (instead of for each element), allowing for volume change within individual elements, but requiring the net volume change for the specimen to be zero. The analyses performed were based on linear strain theory, which is not satisfactory for accurate predictions of stress or displacement at large strain levels, but nonetheless is very useful for comparing various boundary conditions and evaluating their relative influence on stress distributions. If accurate prediction of actual stress magnitudes at large strain levels are important, implementation of a geometrically nonlinear formulation would likely improve results.

Complete end restraint was shown to increase the measured stress-strain response of a linearly elastic specimen with L/D = 1 by as much as 25 percent as compared to frictionless ends. For L/D, the apparent increase in measured stress was approximately 12 percent. Even for interface conditions representative of conventional end platens, the effect of the end friction on measured stress-strain response was much less significant than for the case of complete end restraint. The influence on an elasto-plastic specimen was no different than the influence on a linearly elastic specimen prior to yield. After yield, however, the end friction effects were more significant that those based on linear elasticity. The specimen end friction increases the measured stress for a particular strain level except near the yield point, which is softened by the end conditions because yielding occurs progressively within the specimen. In all cases, the effect of end restraint based on the interface characteristics representative of lubricated end platens was negligible.